nature aging

Technical Report

https://doi.org/10.1038/s43587-024-00747-4

Generation of a selective senolytic platform using a micelle-encapsulated Sudan Black B conjugated analog

Received: 12 June 2024

Accepted: 14 October 2024

Published online: 27 December 2024

Check for updates

Sophia Magkouta[1,2,3,17], Dimitris Veroutis[1,3,17], Angelos Papaspyropoulos[1,17], Maria Georgiou[4,17], Nikolaos Lougiakis[4], Natassa Pippa[5], Sophia Havaki[1], Anastasia Palaiologou[6], Dimitris-Foivos Thanos[1], Konstantinos Kambas[7], Nefeli Lagopati[1,8,9], Nikos Boukos[10], Nicole Pouli[4], Panagiotis Marakos[4], Athanassios Kotsinas[1], Dimitris Thanos[9], Konstantinos Evangelou[1], Fotios Sampaziotis[11,12,13], Constantin Tamvakopoulos[6], Stergios Pispas[14], Russell Petty[3], Nicholas Kotopoulos[1] & Vassilis G. Gorgoulis[1,3,9,15,16]

The emerging field of senolytics is centered on eliminating senescent cells to block their contribution to the progression of age-related diseases, including cancer, and to facilitate healthy aging. Enhancing the selectivity of senolytic treatments toward senescent cells stands to reduce the adverse effects associated with existing senolytic interventions. Taking advantage of lipofuscin accumulation in senescent cells, we describe here the development of a highly efficient senolytic platform consisting of a lipofuscin-binding domain scaffold, which can be conjugated with a senolytic drug via an ester bond. As a proof of concept, we present the generation of GL392, a senolytic compound that carries a dasatinib senolytic moiety. Encapsulation of the GL392 compound in a micelle nanocarrier (termed mGL392) allows for both in vitro and in vivo (in mice) selective elimination of senescent cells via targeted release of the senolytic agent with minimal systemic toxicity. Our findings suggest that this platform could be used to enhance targeting of senotherapeutics toward senescent cells.

Cellular senescence is a stress response mechanism ensuring organismal homeostasis on a transient basis[1]. This cellular state is triggered upon a variety of stress stimuli (oncogenes, telomere shortening/dysfunction, irradiation, chemotherapy, viral infection and others), and individual features depend on cell context and time, rendering senescence a highly variable, heterogeneous and dynamic process. Despite these, senescent cells are, by definition, characterized by four interrelated hallmarks: (1) cell cycle withdrawal, (2) deregulated metabolism, (3) macromolecular damage and (4) a heterogeneous and context-dependent pro-inflammatory secretory profile that includes various mediators (cytokines, chemokines, proteases, growth factors and bioactive lipids), termed senescence-associated secretory phenotype (SASP)[1,2]. Senescent cells remain alive, having ceased cell division, and acquire resistance to apoptosis, although they harbor damage. On a transient basis, senescence contributes to the preservation of homeostasis, as damaged and/or dysfunctional cells are eliminated by immune cells. However, when senescent cells are not properly removed, they may accumulate in tissues and organs over time, perpetuating senescence in a paracrine manner via SASP and altering the tissue microenvironment, overall fostering aging and the development of a variety of age-related disorders, including cancer[1,3]. Interestingly, in the context of carcinogenesis, although beneficial at early stages as a tumor barrier, senescence (oncogene induced or therapy induced) may later on promote cancer progression[4–6]. This 'dark' side of senescence has been attributed to

A full list of affiliations appears at the end of the paper. e-mail: vgorg@med.uoa.gr

https://doi.org/10.1038/s43587-024-00747-4

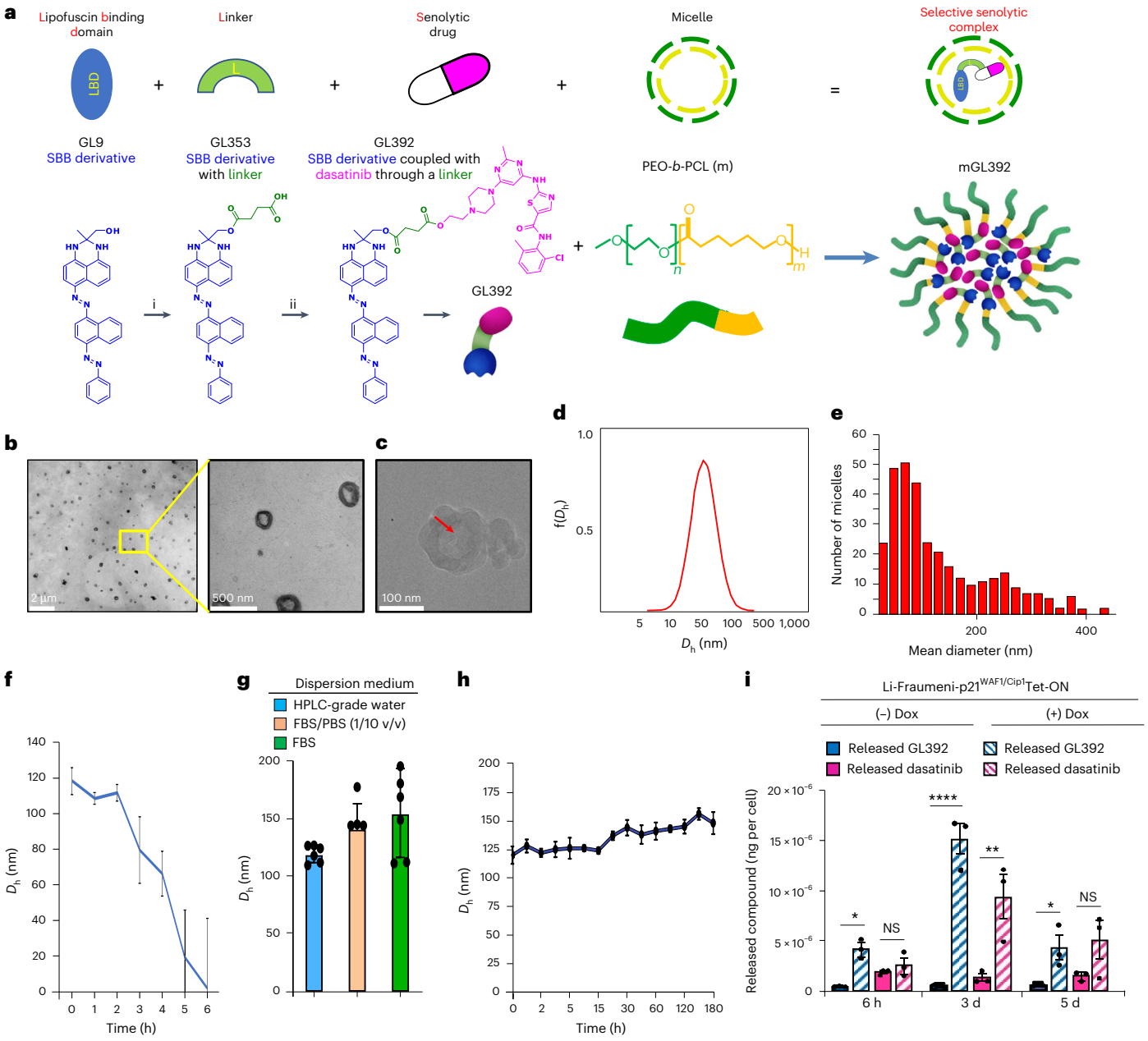

Fig. 1 | The mGL392 compound constitutes a micellated dasatinib-conjugated LBD scaffold for effective targeting of senescent cells. a, Upper panel: the GL392 building platform consists of three regions: the LBD, the senolytic compound and an esteric linker connecting the LBD to the senolytic compound. In the case of GL392, dasatinib was selected as a potent senolytic drug. Lower panel: GL9 contains the LBD and is coupled with dasatinib (purple) through a succinic linker (green) to generate GL392. For more effective dasatinib delivery and specificity, GL392 is encapsulated in PEO-*b*-PCL micelles to create the senolytic mGL392 compound. **b**–**h**, Physicochemical characterization of mGL392. Structure and physicochemical properties of micelle-GL392 were verified using TEM (the yellow inset is magnified on the right frame) (**b**) and cryo-TEM (red arrow indicates the electron-lucent core of mGL392 where GL392 is successfully incorporated) (**c**). Homogeneity of the micelle preparation was verified by evaluation of mGL392 particle distribution based on size (**d**) using DLS and number (**e**) using TEM. Efficient degradation of mGL392 at acidic pH (4.5) was determined by measuring the mean D_h of the particles during a 6-h timecourse using DLS ($n = 3$ independent chemical experiments) (**f**). Stability of the complex in cell culture relevant media was verified at 37 °C ($n = 5$ independent chemical experiments) (**g**) and during the course of a 180-h timeframe ($n = 5$ independent chemical experiments) (**h**) using DLS. **i**, Released GL392 or dasatinib was traced in lysates of senescent (+Dox) or non-senescent (−Dox) Li-Fraumeni-p21$^{WAF1/Cip1}$ Tet-ON cells with LC–MS, after incubation with mGL392 for the indicated time ($n = 3$ biological replicates). *P: 0.01–0.05, **P: 0.001–0.01, ****$P < 0.0001$, two-way ANOVA (**i**). Error bars indicate s.d. NS, non-significant. Data are presented as mean values ± s.d. from at least three independent biological replicates (**f**–**i**).

SASP but, in recent years, also to an alternative mechanism—the 'escape from senescence' phenomenon—that has been proposed to affect the clinical course of patients with cancer[3,6–8]. Taking into account the above, senescent cells have emerged as a therapeutic target to prevent a variety of diseases[9]. Toward this direction, the field of senolytics has rapidly expanded in the last decades[10].

Senolytics are principally approved anti-cancer drugs targeting apoptosis resistance, a key feature of senescent cells[11–13]. Stemming from such drug repurposing strategies, senolytic treatments are frequently accompanied by systemic toxicities and adverse side and off-target effects[11,14]. Thus, bypassing these obstacles by implementing targeted senescent cell clearance emerges as a clinically important

https://doi.org/10.1038/s43587-024-00747-4

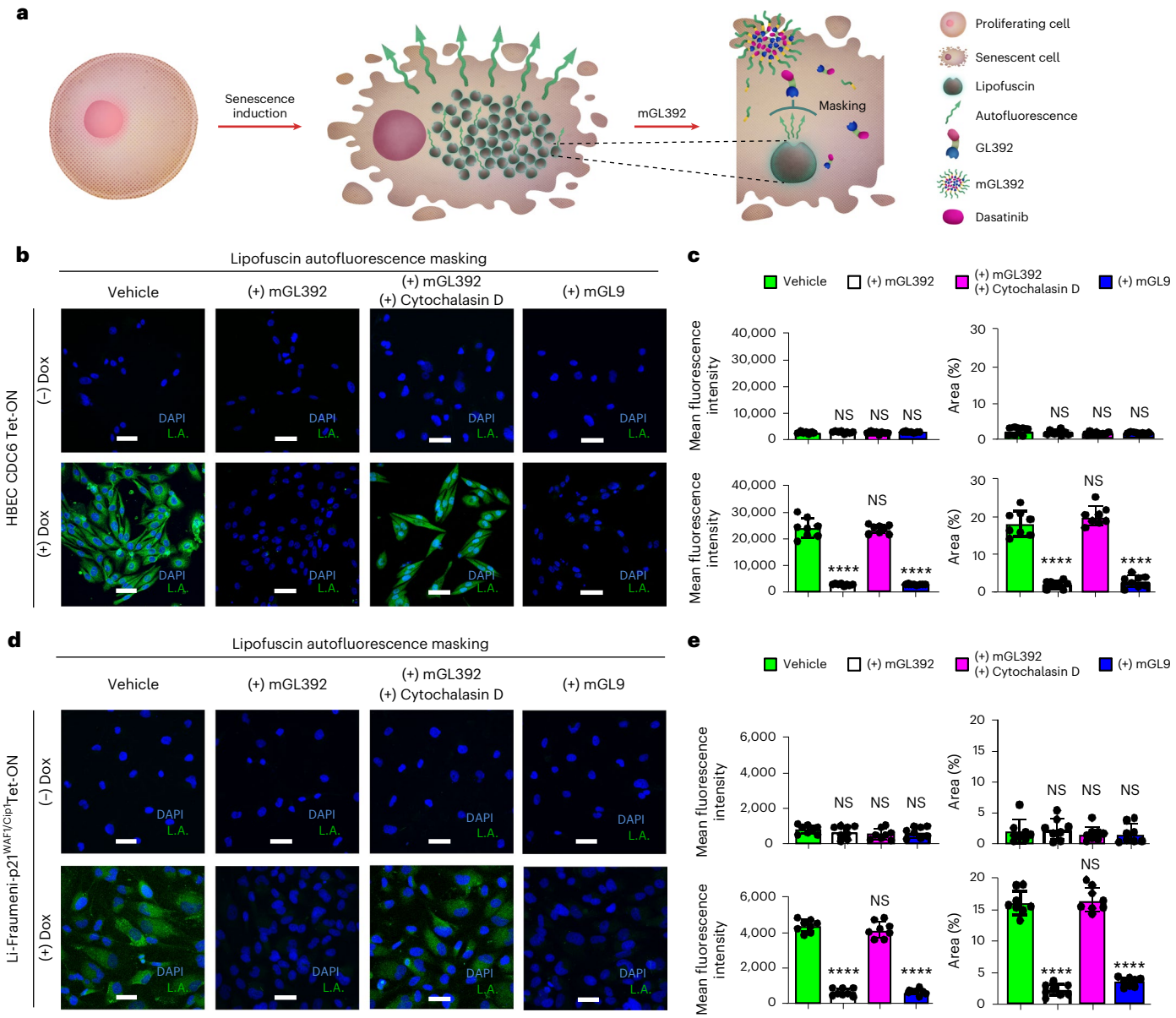

Fig. 2 | The mGL392 compound selectively accumulates within senescent cells. **a**, Proper internalization of mGL392 and specific binding of its cargo to lipofuscin was validated based on lipofuscin auto-fluorescence. During senescence, cells accumulate lipofuscin that emits auto-fluorescence. Upon binding to lipofuscin, mGL392 masks emitted auto-fluorescence signals. **b**, Representative images of senescent (+Dox) or non-senescent (−Dox) HBEC CDC6 Tet-ON, treated or not with cytochalasin D (an actin polymerization inhibitor) and mGL392/mGL9 (10 nM) and evaluated for lipofuscin auto-fluorescence. **c**, Mean fluorescence intensity and percent area of lipofuscin auto-fluorescence in **b** were quantified using ImageJ ($n = 8$ biological replicates). **d**, Representative images of senescent (+Dox) or non-senescent (−Dox) Li-Fraumeni-p21$^{WAF1/Cip1}$ Tet-ON cells, treated or not with cytochalasin D (an actin polymerization inhibitor) and mGL392/mGL9 (10 nM) and evaluated for lipofuscin auto-fluorescence. **e**, Mean fluorescence intensity and percent area of lipofuscin auto-fluorescence in **d** were quantified using ImageJ ($n = 8$ biological replicates). Objective: ×40. Scale bar, 25 µm. **** $P < 0.0001$, one-way ANOVA (statistical denotations represent comparisons to vehicle (PBS)). Error bars indicate s.d. NS, non-significant. Data are presented as mean values ± s.d. from eight independent biological replicates. L.A., lipofuscin autofluorescence.

perspective. Precise recognition of senescent cells is a prerequisite for their selective removal. Despite intense efforts in discovering robust senescence markers, the highly heterogeneous and dynamic nature of senescent cells renders this task truly challenging[1]. Within this context, the only common denominator of senescent cells is lipofuscin—the 'dark matter' of senescence, an auto-fluorescent pigment. Lipofuscin accumulation is an established hallmark of these cells and reflects mainly two of their cardinal features: macromolecular damage and deregulated metabolism[1,15].

Taking advantage of the above, we developed a platform serving as a nanocarrier for selective and precise senolysis. This platform consists of three main parts: (1) a lipofuscin-binding domain (LBD), (2) a linker and (3) a senolytic moiety. As a proof of concept, we chose the established senolytic drug dasatinib, which is currently undergoing clinical trials[12,16], to provide the senolytic moiety. This senolytic compound named GL392 was subsequently enclosed in poly(ethylene-oxide)-block-poly(ε-caprolactone) (PEO-*b*-PCL) micelles for optimal and selective delivery to senescent cells (named mGL392). After physicochemical and functional characterization of the senolytic compound, we extensively evaluated its efficacy in established senescence models. Specifically, we used the two-dimensional (2D) human bronchial epithelial cell (HBEC) CDC6

https://doi.org/10.1038/s43587-024-00747-4

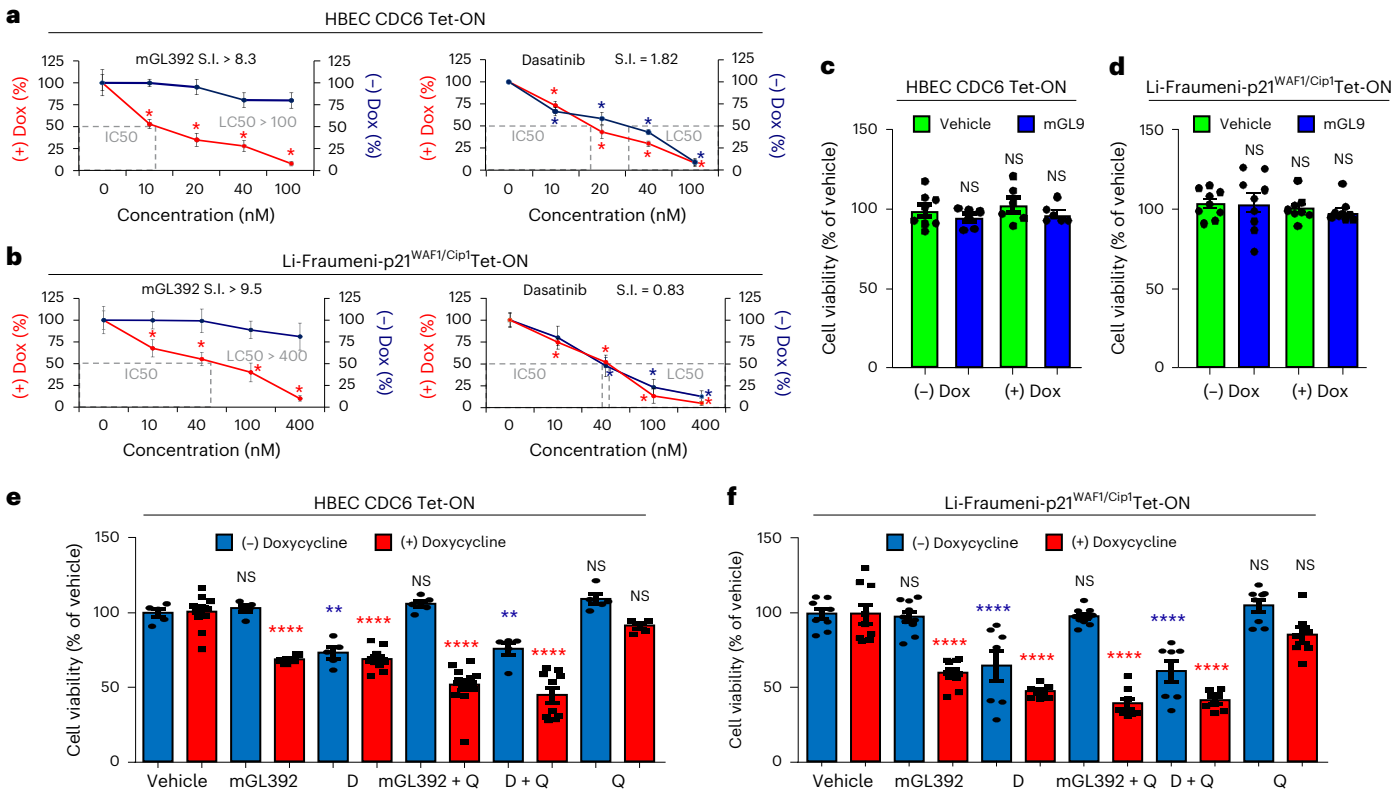

Fig. 3 | Selectivity of mGL392-mediated senolysis is superior to that mediated by free dasatinib. a,**b**, Determination of the selectivity index (SI) for mGL392 compared to free dasatinib in the two inducible cellular senescence systems in HBEC CDC6 Tet-ON (**a**) and Li-Fraumeni-p21WAF1/Cip1 Tet-ON (**b**) cells. In both cases, cells were treated with Dox for senescence entry and subsequently with incremental concentrations of mGL392 (0–400 nM) or free dasatinib (0–400 nM). IC_{50} confers 50% reduction of senescent cells (red line) (senolytic effect), whereas LC_{50} eliminates 50% of non-senescent cells (blue line) (cytotoxic effect). SI was calculated as the LC_{50}/IC_{50} ratio. Data expressed are as percent mean ± s.e.m. of vehicle (PBS), $n = 9$ (biological replicates); blue and red stars represent statistical significance compared to respective (−) and (+) Dox vehicles, $^{*}P < 0.05$ compared to vehicle, one-way ANOVA test. **c**,**d**, GL9 LBD does not exert senolytic or cytotoxic actions. GL9 was encapsulated in a micelle complex and was applied in HBEC CDC6 Tet-ON (**c**) and Li-Fraumeni-p21WAF1/Cip1 Tet-ON (**d**) cells. Cell viability was determined by MTT assay. Data are expressed as percent mean ± s.d. of total cells, $n = 9$ (biological replicates); NS, non-significant compared to respective vehicle (two-sided *t*-test). **e**,**f**, Validation of the senolytic properties of mGL392 in the HBEC CDC6 Tet-ON (**e**) and Li-Fraumeni-p21$^{WAF1/Cip1}$ Tet-ON (**f**) cellular systems. Senescent and non-senescent cells were treated with vehicle (PBS), mGL392 (10 nM in the case of HBEC CDC6 Tet-ON and 20 nM in case of Li-Fraumeni-p21$^{WAF1/Cip1}$ Tet-ON cells) or mGL392+quercetin (mGL392+Q, 10 nM or 20 nM and 10 µM, respectively). Free dasatinib (D, 10 nM and 20 nM for HBEC CDC6 Tet-ON and Li-Fraumeni-p21$^{WAF1/Cip1}$ Tet-ON cells, respectively), quercetin (Q, 10 µM) and free dasatinib+quercetin (D+Q) were used as reference. Cell viability was assessed by MTT assay, 4–6 d after treatment. Results are expressed as mean percent of vehicle ± s.d. Blue and red stars in each condition represent statistical significance compared to (−) and (+) Dox vehicles, respectively. $^{**}P$: 0.001–0.01, $^{****}P < 0.0001$, two-way ANOVA test (**e** and **f**). Error bars indicate s.d. Data are presented as mean values ± s.d, $n = 14$ (biological replicates).

Tet-ON and the Li-Fraumeni-p21$^{WAF1/Cip1}$ Tet-ON cellular systems[17], three-dimensional (3D) patient-derived airway organoids (AOs)[17,18] and the palbociclib-induced senescence murine model[19] to cover both in vitro (2D and 3D) and in vivo settings. Here we provide evidence for its selective and efficient elimination of senescent cells with a negligible impact on normal cells.

The mGL392 compound constitutes a micellated dasatinib-conjugated LBD scaffold selectively released in senescent cells

Given that accumulation of lipofuscin is a universal manifestation of senescent cells, we hypothesized that it could serve as a target for selective elimination of senescent cells. We, therefore, designed an innovative platform serving as a nanocarrier for selective and precise senolysis (Fig. 1a, upper panel). This platform consists of three main parts: (1) an LBD scaffold, (2) a linker and (3) a senolytic moiety. The first part (LBD) is vital for the selective binding of the compound inside senescent cells by anchoring to lipofuscin. The linker is the second component and has a dual role: it not only connects through an ester bond the active drug and the LBD, but it also allows its desirable intracellular cleavage by endogenous esterases that are expressed in abundance[20]. The third region is the most versatile one, as it may consist of any appropriate drug (repurposed or novel) with senolytic activity. Based on the above rationale, we selected GL9 as the most potent LBD, because it was previously shown to exhibit high affinity and selectivity for lipofuscin[21] (Fig. 1a, lower panel) and was previously exploited for the development of biotin-conjugated (GL13) and fluorophore-conjugated (GLF16) compounds able to successfully trace senescent cells in vitro and in vivo[2,17,21]. As a proof of concept, the established senolytic drug dasatinib, which is currently undergoing clinical trials[12,16], was chosen to provide the senolytic moiety. Toward that direction, dasatinib was attached to GL9 via the ester linker, and the resulting compound was termed GL392 (Fig. 1a and Supplementary Note 1). Once GL392 is anchored on lipofuscin, cellular esterases can target this bond[22], eventually releasing active dasatinib. However, GL392 is lipophilic; therefore, a carrier is required for intracellular administration. Thus, we developed PEO-*b*-PCL micelles and incorporated GL392 to increase its solubility via entrapment into micelles. This type of micelle was formulated to preferably degrade within the senescent cell's acidic cytoplasm[23], allowing for efficient and specific

https://doi.org/10.1038/s43587-024-00747-4

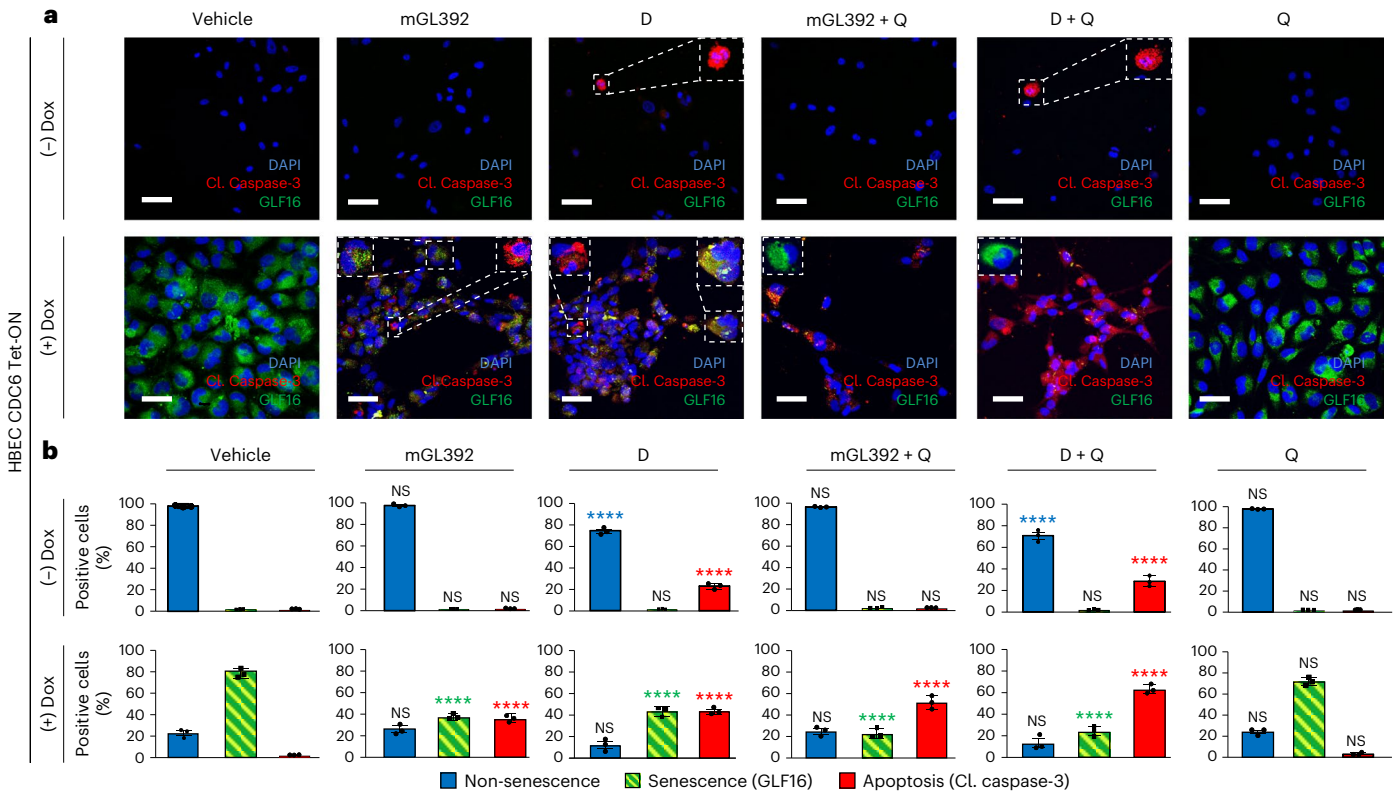

Fig. 4 | mGL392 selectively eliminates senescent cells in vitro in HBEC CDC6 Tet-ON cells. a, Selectivity of mGL392 senolysis was verified by visualization of apoptotic (Cl. Caspase-3$^+$, red) and senescent (GLF16$^+$, green) cells in senescent (+Dox) or non-senescent (−Dox) HBEC CDC6 Tet-ON cells. **b**, Quantification of immunofluorescence in **c**. Blue, green and red stars in each condition represent statistical significance compared to respective (−) and (+) Dox vehicles. Results are expressed as percent positive (senescent or apoptotic) cells counted against DAPI-stained nuclei inspected from at least 10 optical fields per sample ($n = 3$ biological replicates). D, dasatinib; Q, quercetin. Objective: ×40. Scale bar, 25 µm. Blue, green and red stars in each condition represent statistical significance compared to respective (−) and (+) Dox vehicles. Insets represent digital magnifications of representative (indicated) cells within the presented frame. ****$P < 0.0001$, two-way ANOVA test. Error bars indicate s.d. Data are presented as mean values ± s.d. from three independent biological replicates. NS, non-significant.

release of its cargo[23]. Of note, PEO-*b*-PCL micelles are well known for their 'stealth' properties, evading immune recognition while circulating in the bloodstream[24].

After synthesis of the micellar formulation (hereafter referred to as mGL392), we first characterized it physicochemically by measuring the mean hydrodynamic diameter (D_h, nm) and size polydispersity index (PDI) by dynamic light scattering (DLS) as well as its structural features using transmission electron microscopy (TEM) and cryo-TEM (Fig. 1b–e and Supplementary Note 2). Moreover, the stability of mGL392 was demonstrated at pH 7, corresponding to the pH of high-performance liquid chromatography (HPLC)-grade water used as the medium for preparing micelles incorporating GL392 as well as in biomimetic media recapitulating the plasma conditions (Fig. 1f–h and Supplementary Note 2). The stability of mGL392 was also addressed in conditions simulating the acidic intracellular pH of senescent cells (Fig. 1f and Supplementary Note 2). mGL392 remains intact for at least 7 d under standard storage conditions but disassembles within 4–6 h in an acidic environment (Fig. 1f–h and Supplementary Note 2). To gain deeper insight into the intracellular dynamics of mGL392, we evaluated the presence of free GL392 and dasatinib inside senescent and non-senescent cells treated with mGL392 using liquid chromatography–mass spectrometry (LC–MS). In agreement with the degradation data, released dasatinib was detected only in the cytoplasm of senescent cells within 6 h upon initiation of mGL392 treatment. Free dasatinib incrementally accumulated within senescent cells over a 3-d period but could be detected in cell lysates up to 5 d after treatment (Fig. 1i, Extended Data Fig. 1 and Supplementary Note 3).

mGL392 selectively accumulates within senescent cells in vitro by anchoring to lipofuscin and triggering senolysis

Having certified the selective disassembly of the mGL392 complex within senescent cells, we subsequently tested its proper internalization and binding to lipofuscin by evaluating its potential to quench lipofuscin auto-fluorescence (Fig. 2a–e). Indeed, the LBD domain of GL392 retained its strong affinity for lipofuscin (similarly to encapsulated GL9-mGL9 alone that served as positive control) and masked its auto-fluorescent signal (Fig. 2b–e). Internalization of the micelle complex is likely mediated by endocytosis as inhibition of actin polymerization impeded masking (Fig. 2b–e).

We subsequently investigated the potential cytotoxicity of mGL392 using dasatinib as reference (Fig. 3a,b). In this context, half maximal inhibitory concentration (IC_{50}) was determined as the concentration of mGL392 or dasatinib that eliminated 50% of senescent cells, whereas lethal concentration 50 (LC_{50}) eliminated 50% of proliferating control cells. Although mGL392 and dasatinib displayed similar IC_{50} values, the LC_{50} of mGL392 was 2–8 times higher than dasatinib, leading to a substantially higher selectivity index for mGL392 (Fig. 3a,b). This finding implies that mGL392 may offer a considerably larger therapeutic window in the preclinical or clinical settings. Of note, mGL9 alone did not affect cell viability; therefore, the senolytic properties of mGL392 may be solely attributed to released dasatinib (Fig. 3c,d). After determining the appropriate concentration range for mGL392, we thoroughly addressed the senolytic capacity of mGL392 in our two Tet-ON cellular systems. Free

https://doi.org/10.1038/s43587-024-00747-4

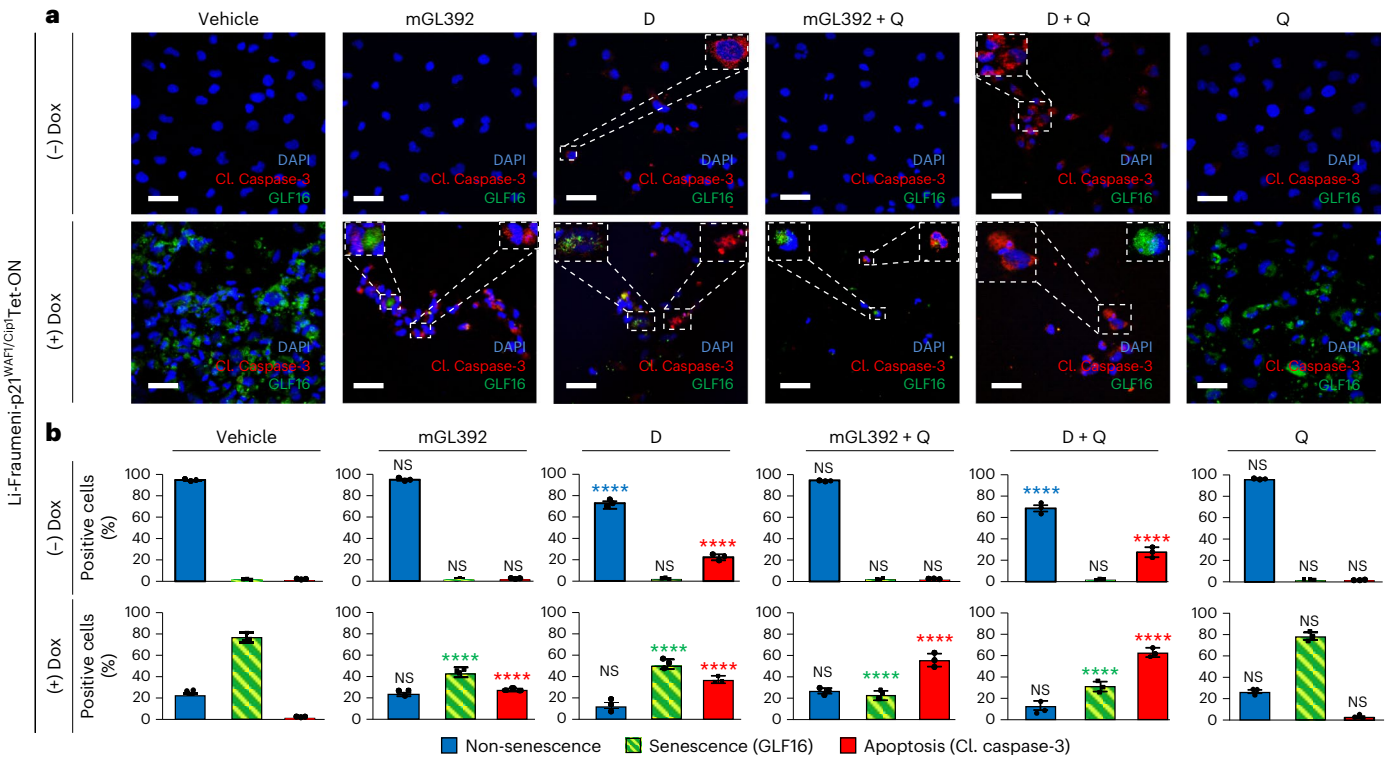

Fig. 5 | mGL392 selectively eliminates senescent cells in vitro in Li-Fraumeni-p21$^{WAF1/Cip1}$ Tet-ON cells. a, Selectivity of mGL392 senolysis was verified by visualization of apoptotic (Cl. Caspase-3$^+$, red) and senescent (GLF16$^+$, green) cells in senescent (+Dox) or non-senescent (−Dox) Li-Fraumeni-p21$^{WAF1/Cip1}$ Tet-ON cells. **b**, Quantification of immunofluorescence in **c**. Blue, green and red stars in each condition represent statistical significance compared to respective (−) and (+) Dox vehicles. Results are expressed as percent positive (senescent or apoptotic) cells counted against DAPI-stained nuclei inspected from at least 10 optical fields per sample ($n = 3$ biological replicates). D, dasatinib; Q, quercetin. Objective: ×40. Scale bar, 25 µm. Blue, green and red stars in each condition represent statistical significance compared to respective (−) and (+) Dox vehicles. Insets represent digital magnifications of representative (indicated) cells within the presented frame. **** $P < 0.0001$, two-way ANOVA test. Error bars indicate s.d. Data are presented as mean values ± s.d. from three independent biological replicates. NS, non-significant.

dasatinib (of equal molarity) or dasatinib combined with quercetin (commonly used together and known to act in a synergistic manner[13]) was used as reference. mGL392 substantially impeded viability of senescent cells either alone or when combined with quercetin in both cellular systems (Fig. 3e,f). Most importantly, mGL392 did not affect viability of non-senescent proliferating cells, an off-target effect that is evident in the case of free dasatinib, both alone or combined with quercetin (Fig. 3e,f). This observation was confirmed by concurrent visualization of senescent and apoptotic cells by immunofluorescence as well as apoptosis/necrosis evaluation by flow cytometry, where selective elimination of senescent cells was achieved upon treatment with mGL392 (alone or combined with quercetin) (Figs. 4a,b and 5a,b and Extended Data Figs. 2 and 3). Again, equal concentrations of free dasatinib severely compromised proliferating HBECs and Li-Fraumeni cells, whereas senescent cell elimination was less effective compared to mGL392 (Figs. 4a,b and 5a,b and Extended Data Figs. 2 and 3).

The senolytic capacity of mGL392 was next challenged in ex vivo 3D organoid cultures generated from healthy lung specimens[18] (Fig. 6a–d and Extended Data Fig. 4). mGL392 was successfully delivered in the 3D setting and conferred a substantial reduction of senescent cells, without affecting proliferating/non-senescent cells, as indicated by both organoid viability and immunofluorescence analyses (Fig. 6a–d and Extended Data Fig. 4). Taken together, these data showcase a selective and highly potent senolytic profile of mGL392 in both 2D and 3D environments, at concentrations that its respective free counterpart (dasatinib) is accompanied by considerable off-target and deleterious effects.

mGL392 enables targeted senolysis in vivo

We subsequently sought to investigate the in vivo efficacy of our innovative compound and challenged its senolytic capacity in the established senescence murine model of palbociclib (CDK4/6 inhibitor)-treated melanoma (Fig. 7a). mGL392 administration substantially eliminated senescent cells robustly induced in melanomas by palbociclib treatment (Fig. 7b,c and Extended Data Fig. 5a,b), accompanied by elevated apoptosis (evaluated by cleaved (Cl.) Caspase-3 levels in tumor sections) (Fig. 7d,e). Given that mGL392 does not suppress proliferating B16 melanoma cells (Fig. 7f) nor tumors when senescence is absent (Fig. 7g), and a substantial reduction of tumor sizes was seen in mice treated with both palbociclib and mGL392 (Fig. 7h,i and Extended Data Fig. 5c), the observed anti-tumor effects of mGL392 may be attributed only to selective senolysis. On the contrary, free dasatinib administration resulted in reduced cell viability even in the absence of senescence (Fig. 7f). Of note, tumors formed in mGL392 (+palbociclib)-treated mice were considerably smaller than those treated with dasatinib (+palbociclib) or combined dasatinib and quercetin (+palbociclib) (Fig. 7h). Quercetin administration did not improve the efficacy of dasatinib or mGL392 (Fig. 7b–e,h). Apart from the substantially lower efficiency in tumor inhibition, dasatinib administration was accompanied by a deregulation of serum markers associated with liver function, such as alkaline phosphatase (ALP) and aspartate transaminase (AST)/alanine transaminase (ALT) ratio, as well as creatinine phosphokinase (CPK), a marker of muscle injury (Extended Data Fig. 5d), in line with previous studies[25–27]. In contrast, no signs of mGL392-mediated toxicity were found in mouse sera or upon histopathological evaluation (Extended Data Fig. 5d,e). Lastly, to verify the 'stealth' properties of mGL392

https://doi.org/10.1038/s43587-024-00747-4

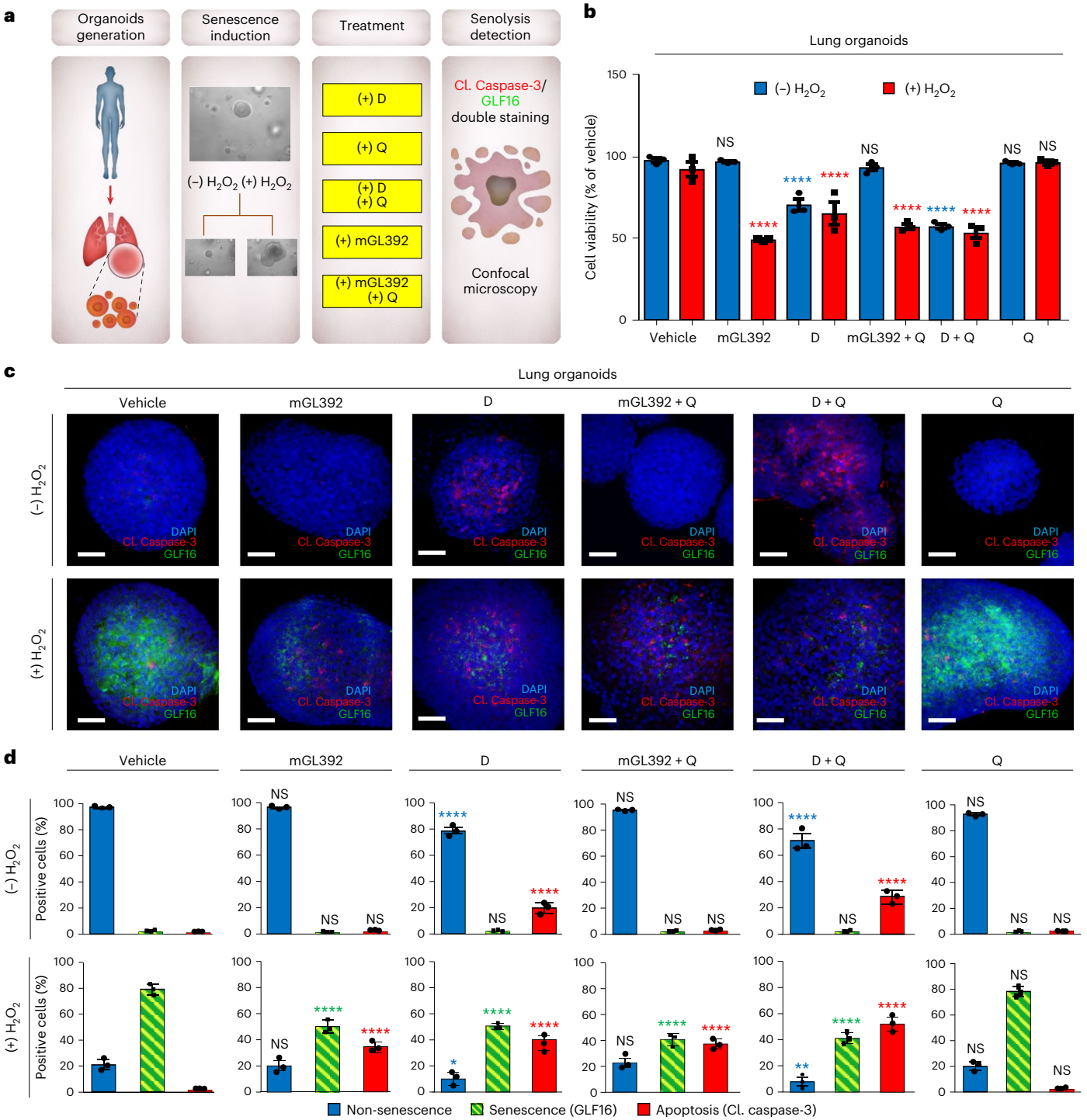

Fig. 6 | mGL392 induces targeted senolysis in 3D patient-derived lung organoids. a, Overview of the experimental workflow. AOs were generated from surgically resected healthy lung tissue. Organoid cultures were treated with H_2O_2 for senescence induction or left untreated. In both cases, the organoid medium was supplemented with vehicle (PBS), mGL392 (500 nM), dasatinib (D, 500 nM), quercetin (Q, 10 µM), dasatinib and quercetin (D+Q) or mGL392 and quercetin (mGL392+Q) for 4 d. Selective senolysis was evaluated by cell viability measurements and quantification of senescent and apoptotic cells by immunofluorescence. **b**, Organoid cell viability was determined using a proteasome activity assay. Results are presented as percent of vehicle. Blue and red stars in each condition represent statistical significance compared to (−) and (+) H_2O_2 vehicles, respectively ($n = 3$ biological replicates). **c**,**d**, Apoptosis (Cl. Caspase-3 immunoreactivity, red) and senescence (GLF16 staining, green) assessment was performed to verify the selective senolytic activity of mGL392. **c**, Representative images of confocal microscopy. Objective: ×20. Scale bar, 10 µm. **d**, Quantification of immunofluorescence analysis in **c**. Results are expressed as percent positive (senescent or apoptotic) cells counted against DAPI-stained nuclei inspected from at least 10 optical fields per sample ($n = 3$ biological replicates). Blue, red and green stars in each condition represent statistical significance compared to respective (−) and (+) H_2O_2 vehicles. **P*: 0.001–0.05, ***P*: 0.001–0.01, *****P* < 0.0001, two-way ANOVA test. Error bars indicate s.d. Data are presented as mean values ± s.d. from three independent biological replicates. NS, non-significant.

https://doi.org/10.1038/s43587-024-00747-4

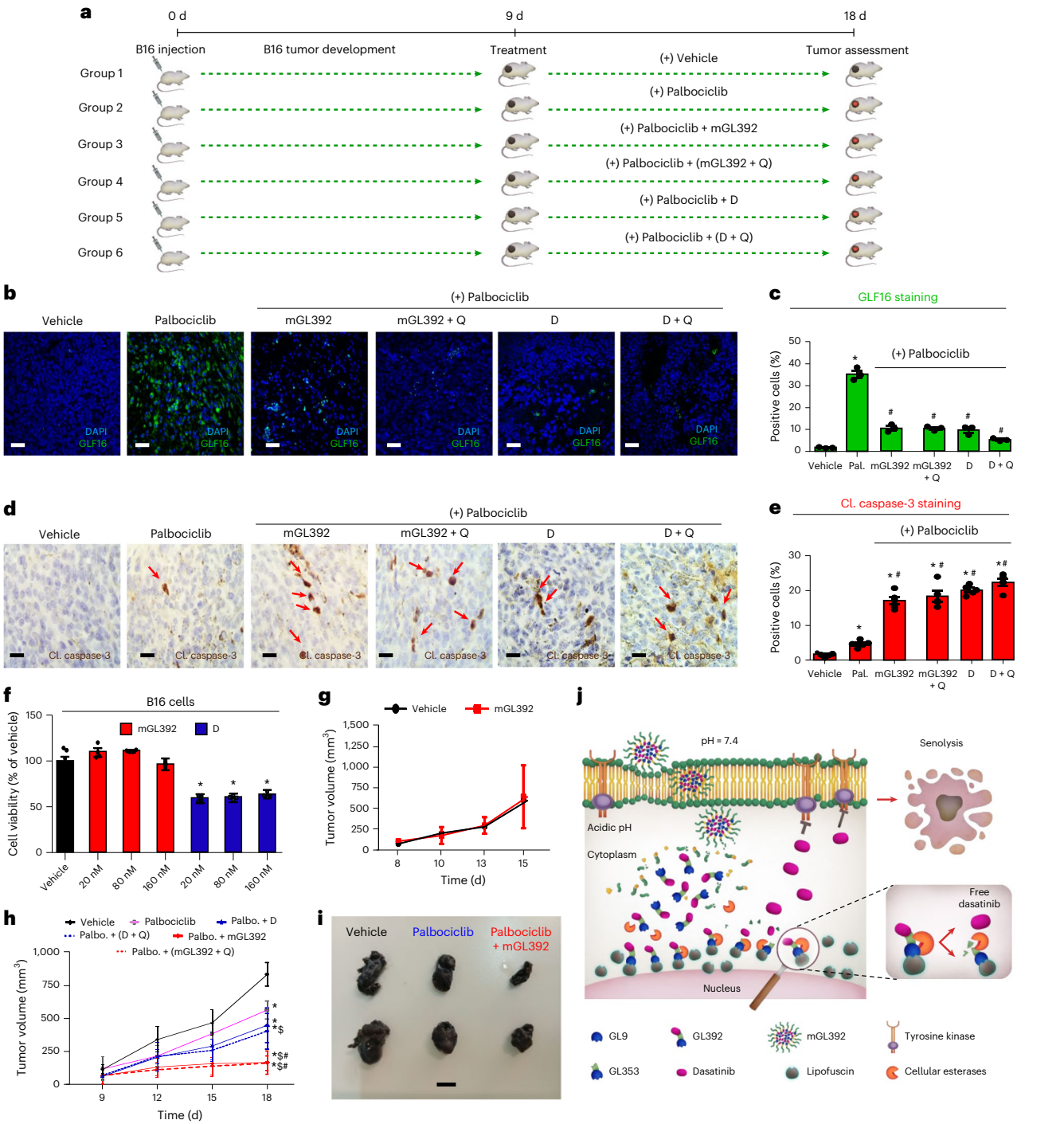

Fig. 7 | mGL392 enables efficient delivery and selective release of the senolytic agent in vivo. a, The in vivo mGL392 senolytic potential was challenged in a murine model of palbociblib-induced senescence. Timeline of in vivo experiment. Murine melanomas developed upon subcutaneous injection of B16 cells. Mice were split into six groups and received vehicle (normal saline), palbociclib (Pal.), palbociclib/mGL392 (mGL392), palbociclib/mGL392/quercetin (mGL392 + Q), palbociclib/dasatinib (D) and palbociclib/dasatinib/quercetin (D + Q) daily for 9 d. Palbociclib was administered at 2.5 mg per mouse, mGL392 at 0.015 mg per mouse, dasatinib at 0.125 mg per mouse and quercetin at 1.25 mg per mouse. **b**,**c**, Representative immunofluorescence images displaying senescent cells (GLF16$^+$, green) (**b**) and quantification of senescent cell populations in the tumors (**c**). Results are expressed as percent positive senescent cells counted against DAPI-stained nuclei from at least 10 inspected optical fields per sample. Data are presented as mean values ± s.d. of total cells, $n = 5$ (biological replicates), $^*P < 0.05$ compared to vehicle, $^{\#}P < 0.05$ compared to the palbociclib group by one-way ANOVA. Objective: ×20. Scale bar, 10 µm. **d**,**e**, Effective mGL392-mediated senolysis leads to enhanced tumor cell apoptosis. Representative images of Cl. Caspase-3 staining (cells depicted by red arrows) (**d**) and quantification of analysis (**e**). Results are expressed as percent mean ± s.d. of total cells, $n = 5$ (biological replicates), $^*P < 0.05$ compared to vehicle, $^{\#}P < 0.05$ compared to the palbociclib group by one-way ANOVA. Data are presented as mean values ± s.d. Objective: ×20. Scale bar, 10 µm. **f**,**g**, mGL392 does not affect non-senescent B16 melanoma growth in vitro ($n = 4$ biological replicates) (**f**) or in vivo ($n = 6$ biological replicates) (**g**), as assessed by MTT cell viability and tumor size measurements, respectively. Results are expressed as mean ± s.d., $^*P < 0.05$ compared to vehicle by one-way ANOVA. Data expressed are presented as mean values ± s.d. **h**, mGL392 enhances the melanoma-reducing action of palbociclib. Tumor sizes were measured every 3 d. Data are presented as mean values ± s.e.m., n = 8 (biological replicates), $^*P < 0.05$ compared to vehicle, $^{\#}P < 0.05$ compared to dasatinib, $^{\$}P < 0.05$ compared to palbociclib by one-way ANOVA. **i**, Representative tumors from **h**. Scale bar, 5 mm. **j**, Proposed model of mGL392 action. Palbo., palbociclib.

in vivo, we assessed potential changes in the population of circulating monocytes in animals treated with mGL392 compared to controls. No onsiderable differences were found between the two groups (Extended Data Fig. 5f), indicating the absence of senolytic effects on phagocytes.

In conclusion, we present a delivery platform allowing targeted in vitro and in vivo selective senolysis, whose mode of action can be summarized as follows. Micelle encapsulation facilitates GL392 cellular internalization and favors its selective release in senescent cells, as it preferably disintegrates upon exposure to the low cytosolic pH of senescent cells. The discharged GL392 accumulates inside senescent cells due to its high affinity for lipofuscin, and its ester linker is subsequently hydrolyzed by intracellular esterases to effectively release dasatinib, overall promoting senolysis (Fig. 7j).

Discussion

We present a platform capable of extremely selective and precise senolysis, consisting of the following components: (1) an LBD, (2) a linker and (3) a senolytic moiety. By implementing GL9 and dasatinib as an LBD and senolytic drug, respectively, we generated the GL392 compound. Subsequent encapsulation of GL392 inside a 'senescent cell-sensitive' nanocarrier led to formulation of the mGL392 complex, a cell-permeable and highly potent senolytic tool.

Our data render mGL392 an effective strategy for selective senolysis, overcoming many of the challenges accompanying previously developed approaches. Those approaches relied heavily on lysosomal senescence-associated β-galactosidase (SA-β-gal) activity degrading a galacto-oligosaccharide-coated nanoparticle carrying a senolytic agent or activating via hydrolysis a β-galactosidase-targeted prodrug[28]. However, increased SA-β-gal activity is not specific for senescence, and its use frequently results in false-positive or false-negative outcomes[15,29]. Moreover, low tissue penetration for these delivery systems has been reported[30]. Other approaches that have been tested for senolysis include (1) nanoparticles carrying a monoclonal antibody against the CD9 receptor and CD9-targeted PEGylated liposomes, both carrying the mTOR inhibitor rapamycin that reduces senescence; (2) molybdenum disulfide (MoS2) nanoparticles facilitating autophagy and suppressing senescence; (3) docetaxel–tannic acid self-assembly (DSA)-based nanoparticles delivering docetaxel, a TGFβR1/FOXO1/$p21^{WAF1/Cip1}$ axis inhibitor; (4) β2 microglobulin (B2M) nanoparticles loaded with dasatinib; (5) quercetin surface-functionalized magnetite nanoparticles (MNPQ); and (6) immune system-mediated strategies[28,30]. Again, these systems depend on non-specific to senescence features, such as CD9, B2M, CD153 and urokinase-type plasminogen activator receptor (uPAR) surface expression, and are followed by severe drawbacks stemming from side effects, less biocompatible concentrations, defective drug encapsulation and nanocarrier absorption, interference with human metabolism, problematic distribution and low ligand conjugation efficacy[28,30].

Although lipofuscin is known to accumulate in senescent cells, this may also happen with age in some tissues harboring post-mitotic cells, such as the neural tissue, heart and skeletal muscle[31]. In post-mitotic cells, lipofuscin accumulation may signify cellular senescence characterized as post-mitotic senescence[32,33]. Under this prism, elimination of such cells from aged tissues with the mGL392 platform would turn out beneficial for the organism, as those dysfunctional cells produce a variety of factors (SASP) leading to age-related disease[1]. For instance, systemic senolysis by genetic means in preclinical models was shown to be effective against sarcopenia[12,34]. However, even in the case where aged cells do accumulate some lipofuscin levels due to damage aggregation and decline in metabolic and other processes, the micelle would have to disintegrate within those cells, provided they are acidic, eventually releasing dasatinib, but it is unlikely that the drug would exert senolytic activity, as that would require targeting one or more anti-apoptotic pathways inherent to senescent cells (senescent cell anti-apoptotic pathways (SCAPs))[12].

As far as compound pharmacokinetics is concerned, this primarily relates to the plasma levels of active pharmaceutical ingredients (APIs). The pharmacokinetics of an API, which, in our case, is GL392, is strongly affected by the behavior of the micelles in the human plasma. Pharmacokinetics and tissue distribution of APIs encapsulated in PEO-*b*-PCL micelles have been described in the literature[35,36]. According to the findings, pinocytosis was the main mechanism of cellular absorption of the drug-loaded micelles, leading to a pharmacokinetic profile that was similar to commercially available pharmaceutical products incorporating the same API[35,37]. Furthermore, intratumor administration of PEO-*b*-PCL encapsulating cytostatic active substances resulted in low drug levels in animal serum while maintaining high levels within the tumor[38]. Due to the stealth properties of the PEO-*b*-PCL micelle, the prepared micellar formulations remain intact after intravenous administration[39,40]. The latter ensures zero to low levels of GL392 in the serum while achieving considerable high drug levels in the acidic cytoplasm of senescent cells and senolysis, as also confirmed by our LC–MS analysis. For our study, we deduce that mGL392 bears a pharmacokinetic profile similar to what has been previously described, given that the carrier is already well characterized in such settings.

The rapidly developing field of senotherapeutics, and particularly senolytics, comprises a promising approach to eliminate senescent cells as a strategy to deal with aging and age-related diseases. Despite the importance of senescent cells in age-related and chronic diseases[41–43] and the benefits from their clearance[34], senotherapeutics still faces several unresolved issues. Consistent with the heterogeneity of senescent cells, the efficacy of senolytics varies in a cell-dependent and concentration-dependent manner[44] and is accompanied by adverse (for example, thrombocytopenia and neutropenia[45]) or off-target effects. Even dasatinib, currently the most established senolytic, is associated with various adverse effects[12,26], severely compromising the viability of non-senescent cells (Figs. 3a,b,e,f and 4–6 and Extended Data Figs. 2–4). Our platform successfully addresses all the above issues while exerting, at the same time, a broad spectrum of applicability to alleviate any type of senescence, irrespective of stimulus and cell context. Importantly, in the case of cancer treatment, although most of the proliferating cancer cells are eliminated by traditional anti-cancer therapeutics, a residual population that undergoes therapy-induced senescence may emerge[46,47]. This population needs to be eliminated by senolytic means as a complementary strategy to conventional cancer treatments, given that therapy-induced senescent cancer cells can 'escape' and re-enter the cell cycle while acquiring more aggressive traits, overall fueling tumor relapse and poor clinical outcome[6,48].

Conclusively, the presented platform comprises an innovative, clinically tolerant tool for the design and targeted delivery of senolytic compounds, thereby offering a viable approach for clinical manipulation of senescence-associated diseases.

Methods

Chemical synthesis of the hybrid compound GL392

GL392 was synthesized as follows. First, the hydroxylated on the methyl group of the perimidine ring Sudan Black B (SBB) analog GL9 (described in Evangelou et al.[21]) was treated with succinic anhydride, using 4-dimethylaminopyridine (DMAP) as a base, resulting in the SBB derivative GL353 that carries the succinic linker. The SBB-linker intermediate was subsequently coupled with dasatinib in the presence of *N*,*N*′-dicyclohexylcarbodiimide (DCC) leading to the GL392 derivative. Detailed synthesis and characterization of GL392 is provided in Supplementary Note 1.

Preparation of micelles

Polymeric micelles were prepared by the thin-film hydration method as previously described[49]. A detailed description regarding the preparation of PEO-*b*-PCL micelles is provided in Supplementary Note 2.

Physiochemical characterization of mGL392

DLS. The physicochemical characteristics of the prepared nanosystems were evaluated by measuring their mean D_h (nm) and size distribution through DLS. A detailed description concerning the characterization of pure PEO-*b*-PCL and mGL392 is provided in Supplementary Note 2.

TEM. The morphological observation of the nanosystems was achieved through TEM analysis that also supported the successful incorporation of GL392 into polymeric carriers. The number and size distribution of the nanosystems was obtained also through TEM analysis. A detailed description concerning the characterization of pure PEO-*b*-PCL and mGL392 is provided in Supplementary Note 2. The morphology of the nanosystems was also feasible, applying cryo-TEM (JEOL 2100Plus), operated at 200 keV and equipped with LaB_6 filament. Cryo-samples were observed under low-dose conditions (30 e/Å^2) using SerialEM software. A detailed description concerning the characterization of pure PEO-*b*-PCL and mGL392 is provided in Supplementary Note 2.

In vitro and ex vivo models

The following cellular models were employed:

i. 2D: The Li-Fraumeni-p21$^{WAF1/Cip1}$ Tet-ON and HBEC CDC6 Tet-ON cellular systems developed by our team were used in all in vitro experiments. Li-Fraumeni-p21$^{WAF1/Cip1}$ Tet-ON cells were maintained in DMEM, 10% tetracycline-free FBS and 1% penicillin–streptomycin solution, and HBEC CDC6 Tet-ON cells were maintained in keratinocyte serum-free medium (Invitrogen, 17005–075) supplemented with 50 μg ml^{-1} bovine pituitary extract and 5 ng ml^{-1} hEGF (Invitrogen, 17005–075). Senescence entry was accomplished upon addition of doxycycline (Dox) (10 μg ml^{-1}) (AppliChem) replenished every 2 d for 6 d (refs. 3,21).

ii. B16 murine melanoma cells were purchased from the American Type Culture Collection and maintained in DMEM, 10% FBS supplemented with 2 mM L-glutamine and 1% penicillin–streptomycin solution.

iii. 3D: AOs were generated from lung tissue surgically resected from patients with non-small cell lung cancer and cultured as described previously[18]. In brief, collection of tissues for the generation of AOs was carried out according to European Network of Research Ethics Committees guidelines and the local NKUA Medical School Bioethics Committee (protocol number: 571). All organoid lines were generated from patients who signed informed consent forms, and their personal information remained anonymous.

Palbociclib-induced senescence murine melanoma model

C57BL/6 male and female mice (6–8 weeks old) were purchased from the Biomedical Sciences Research Center Alexander Fleming Institute and housed at the Animal Model Research Unit of Evangelismos Hospital under a 12-h light/dark cycle at 22.5 °C temperature and 55% humidity, receiving food and water ad libitum. Animals were acclimatized for 10 d before experiments. Mouse experiments were approved by the Veterinary Administration Bureau, Prefecture of Athens, Greece (decision number: 854066, 15/07/2023) under compliance with national laws and European Union directives. Sample size was determined upon power analysis using G*Power software[50] (setting significance 0.05, effect size *f* 0.89 and power 0.80). In brief, mice were sex and age matched, and melanoma tumors were generated upon subcutaneous injection of 5×10^5 cells per 100 μl of PBS in the right flank of 8–10-week old C57BL/6 syngeneic mice. Once tumors became palpable (8–9 d after tumor cell inoculation), mice were split by simple randomization into six groups receiving vehicle (normal saline), palbociclib (CDK4/6 inhibitor, PD-0332991), palbociclib and mGL392, palbociclib and dasatinib, palbociclib and dasatininib and quercetin, palbociclib and mGL392 and quercetin. Quercetin was not found to affect tumor size in vehicle-treated or palbociclib-treated mice and was omitted from the experimental design. Palbociclib was administered at 2.5 mg per mouse and mGL392 at 0.015 mg per mouse. Dasatinib was administered at 0.125 mg per mouse and quercetin at 1.25 mg per mouse. The mGL392 dosage was selected based on the reported administered dose of free dasatinib (5 mg kg^{-1} body weight) in senolytic studies[12,51,52] and its bioavailability (approximately 14%; ref. 53). Palbociclib and quercetin were administered by oral gavage and mGL392 and dasatinib intraperitoneally. Administration was performed daily for nine consecutive days. Tumors were monitored daily and measured every 2–3 d using a caliper. Tumor sizes were calculated using the following formula: width^2 × length / 2; and results were expressed in mm^3. Mice were euthanized (humane endpoint was set for tumor volume below 2×10^3 mm^3 or any sign of distress) by sevoflurane overdose; blood was collected; and tumors, vital organs and hindlimb muscles were excised and fixed in formalin for subsequent analysis.

Cell viability assays

Li-Fraumeni-p21$^{WAF1/Cip1}$ Tet-ON or HBEC CDC6 Tet-ON cells were seeded at 8×10^3 cells per well in 96-well plates. Senescence was induced by Dox treatment (0.01 mg ml^{-1}) for 6 d (media refreshed every 2 d). One day before Dox induction, Li-Fraumeni-p21$^{WAF1/Cip1}$ Tet-ON or HBEC CDC6 Tet-ON cells were prepared (at 10×10^3 cells per well) to serve as non-senescent counterparts. In both cases, the cell medium was subsequently removed, and cells were treated with vehicle, mGL392 (10–20 nM), dasatinib (Merck, SML2589) (10–20 nM), quercetin (Merck, 84906-978) (10 μM), dasatinib and quercetin or mGL392 and quercetin for 4 d (in the case of HBEC CDC6 Tet-ON) or 6 d (in the case of Li-Fraumeni-p21$^{WAF1/Cip1}$ Tet-ON). Cell viability was determined by MTT (3-(4,5-Dimethylthiazol-2-yl)-2,5-diphenyltetrazolium bromide) assay (Merck, M5655) applied at 0.5 mg ml^{-1} for 3 h.

In the case of B16 cells, they were seeded at 3×10^3 cells per well in 96-well plates, and, 24 h later, the medium was removed and cells were treated with mGL392 (20–160 nM) or dasatinib (20–160 nM) for 4 d. Cell viability was assessed by MTT assay as mentioned above.

Organoids were treated (or not) with 150 μM hydrogen peroxide (H_2O_2) for 72 h (replaced daily) to induce senescence and then cultured for another 48 h in H_2O_2-free medium. Organoids were then filtered using 70-μm strainers (Corning) to avoid formation of necrotic cores and subsequently treated with vehicle, mGL392 (500 nM), dasatinib (500 nM), quercetin (10 μM), dasatinib and quercetin or mGL392 and quercetin for 4 d in 5% basement membrane extract (BME)/AO medium. Cell viability was evaluated with CellTiter-Fluor Cell Viability Assay reagent (Promega, G6081), according to the manufacturer's instructions.

Immunofluorescence

Li-Fraumeni-p21$^{WAF1/Cip1}$ Tet-ON and HBEC CDC6 Tet-ON cell lines were seeded (2×10^4 cells per well) in 24-well plates over coverslips. Senescence induction was achieved by a 6-d Dox treatment (10 μg ml^{-1}). Senescent and respective non-senescent counterparts were treated as described above for 4–6 d. Cell culture medium was removed, and coverslips were washed and fixed using 4% PFA/PBS for 10 min at 4 °C. Cells were permeabilized by applying Triton X-100 0.3%/PBS for 15 min at room temperature.

In the case of organoids, they were initially retrieved from BME using appropriate medium (Cell Recovery Solution, Corning), washed with PBS, fixed for 20 min in 4% PFA and permeabilized using 0.2% Triton X-100 for 20 min.

In the case of tissue, we obtained 4-μm-thick sections and de-paraffinized and hydrated them. Antigen retrieval was performed by immerging the samples into a citric acid buffer (pH 6) for 18 min in a steamer. Tissue samples were cooled down and washed with PBS.

In all three cases, blocking of non-specific epitopes was performed using normal goat serum (Abcam, ab7481) in 1:40 dilution (in PBS) for 1 h at room temperature. Cells, organoids or tissue specimens were

incubated with primary antibody (Cl. Caspase-3, 1:400; Cell Signaling Technology (CST), 9661) for 1 h, and positive cells were visualized using secondary goat anti-rabbit IgG H&L antibody (Alexa Fluor 488; 1:500; Abcam, ab150077, polyclonal) for 1 h. Upon staining with primary and secondary antibodies, cells, organoids and tissue sections were stained for lipofuscin using GLF16 for 10 min (60 μg ml^{-1}) in the dark. Excess compound was removed by washing three times with the GLF16 diluent (2.5% DMSO/2.5% Tween 20/PBS). Nuclei were finally visualized by DAPI staining. Cells, organoids or tissue samples were washed (30 s with dH_2O), and coverslips were mounted onto slides for microscopy (Supplementary Figs. 4 and 5). Samples were imaged on a Leica TCS-SP8 confocal microscope.

SA-β-gal staining

SA-β-gal was evaluated in Li-Fraumeni-p21$^{WAF1/Cip1}$ Tet-ON and HBEC CDC6 Tet-ON cells seeded at a density of 2×10^4 cells per well in 24-well plates onto coverslips. Senescence was induced by a 6-d Dox treatment (10 μg ml^{-1}). Senescent and respective non-senescent counterparts were treated as described above for 4–6 d. The supernatant was then removed, and cells were washed with PBS and fixed and stained using a Senescence β-Galactosidase Staining Kit (CST, 9860).

For SA-β-gal evaluation, freshly excised B16 tumors from all mouse groups were flash frozen and subsequently embedded in OCT and kept at −80 °C. Cryosections (10 μm) were fixed in 1% formaldehyde solution for 2 min, and tissue sections were incubated with X-gal staining solution (Senescence β-Galactosidase Staining Kit; CST, 9860) for 24 h and visualized on a Zeiss Axiolab 5 microscope.

Quenching of lipofuscin autofluorescence

HBEC CDC6 Tet-ON or Li-Fraumeni-p21$^{WAF1/Cip1}$ Tet-ON cells were seeded at 4×10^4 cells per well in 12-well plates. Senescence induction was achieved by a 6-d Dox treatment (10 μg ml^{-1}). Senescent and respective non-senescent counterparts were cultured with vehicle (PBS) or cytochalasin D (Merck, C8273) (0.5 μM) (for actin polymerization inhibition) for 30 min, and, subsequently, 83 ng ml^{-1} mGL392 or mGL9 was added and incubated overnight. Cell media were subsequently removed; cells were washed with PBS and fixed with 4% PFA for 15 min; and nuclei were visualized by DAPI. Lipofuscin autofluorescence was detected under the RFP EVOS cube (593/40 nm). Mean fluorescence intensity and percent area were determined by ImageJ.

Immunohistochemistry

Formalin-fixed B16 melanoma tumors were embedded in paraffin, and 4-μm sections were analyzed for the presence of apoptotic cells via Cl. Caspase-3 staining. In brief, sections were de-paraffinized and hydrated. Antigens were retrieved using pre-heated citric acid buffer (pH 6) for 18 min. Samples were cooled down into an ice bath for 20 min, washed with TBS and treated with 3% H_2O_2 (cat. no. K5007) for blocking of endogenous peroxidase for 18 min at room temperature. Non-specific binding sites of the primary antibody were blocked by applying normal goat serum (1:40; Abcam, ab7481) for 1 h at room temperature. Tissue sections were washed with PBS and incubated with the primary anti-cleaved Caspase-3 (1:400; CST, 9661) antibody overnight at 4 °C. Samples were washed with TBS, and the positive signal was achieved using a Dako REAL 140 EnVision Detection System (cat. no. K5007) according to the manufacturer's instructions. Tissue specimens were counterstained with hematoxylin. Samples were observed under a Zeiss Axiolab 5 microscope on the ×10 and ×20 objectives and evaluated by two independent experienced pathologists. Variability was minimal among blinded observers ($P < 0.005$).

For the assessment of organ histopathological features, muscle, lung, heart, spleen, liver and kidneys from all groups were fixed and embedded in paraffin, and 4-μm sections were stained by hematoxylin and eosin for visualization of organ microanatomy. Histopathological evaluation was performed by two independent experienced pathologists.

Annexin V/propidium iodide assay

mGL392-induced senolytic activity was evaluated via flow cytometry–based apoptotic assessment upon staining with Annexin V/propidium iodide (PI). In brief, HBEC CDC6 Tet-ON or Li-Fraumeni-p21$^{WAF1/Cip1}$ Tet-ON cells were seeded at 2×10^5 cells per well in six-well plates and treated with Dox to induce senescence. Senescent and respective non-senescent counterparts were subsequently treated as described above for 4–6 d. The supernatant was removed, and cells were washed with PBS and stained with Annexin V-FITC and PI for evaluation of apoptotic and dead cells, respectively, using the FITC Annexin V Apoptosis Detection Kit with PI (BioLegend, 640914) (Supplementary Fig. 6). Flow cytometry data were analyzed using FlowJo software version 10.8.1.

LC–MS

Li-Fraumeni-p21$^{WAF1/Cip1}$ Tet-ON cells were seeded in 10-cm culture plates up to 70% confluency. Senescence was induced by Dox treatment (0.01 mg ml^{-1}) for 6 d (media refreshed every 2 d). mGL392 (20 nM) was subsequently added, and cells were incubated from 6 h to 5 d. Cells were washed twice with PBS (to remove mGL392) and lysed using 9 ml of acetonitrile/water (ACN:H_2O) (3:2) cold solution. Then, 200 μl of this solution was subsequently used for LC–MS analysis. Standard prepared solutions of dasatinib and GL392 were used, and lapatinib was also used as internal control. Results were quantified based on the standard curves and normalized to the total number of cells. Detailed information of the LC–MS analysis is presented in Supplementary Note 3.

Blood and sera analysis

Blood from mice bearing B16 melanomas treated with vehicle or mGL392 was collected and centrifuged at 1,000*g* for 15 min, and sera were obtained and sent to an external certified veterinary laboratory (Vet In Progress (https://vetinprogress.gr/en/)) for quantification of the following markers associated with vital organ damage: creatinine (CREA), albumin (ALB), total protein (TP), ALP, total bilirubin (TBIL), globulins, gamma-glutamyl transferase (γ-GT), AST, ALT, CPK and blood urea nitrogen (BUN).

Alternatively, the cell pellet was resuspended in Red Blood Cell lysis solution (BioLegend), and white blood cells were collected upon centrifugation at 400*g* for 10 min. Cells were stained with anti-CD45-APC-Cy7 (clone 30-F11, 103115), CD11b-FITC (101205, clone M1/70), F4/80-PerCP (123125, clone BM8) and Ly6C-PE (128007, clone HK1.4) at a 1:100 dilution (all from BioLegend), for quantification of circulating monocytes and macrophages, and samples were analyzed by flow cytometry (Supplementary Fig. 6).

Statistics and reproducibility

All data are presented as means ± s.d. or means ± s.e.m., as indicated. Differences between groups were evaluated using the parametric two-tailed Student's *t*-test, two-way ANOVA or one-way ANOVA with Bonferroni's post hoc test for multiple comparisons, as appropriate. $P < 0.05$ was considered significant. Graphs, calculations and statistical analyses were performed using GraphPad Prism version 10.0 (GraphPad Software). All statistical tests included a check for normality of analyzed data. Data measurements and detailed statistical analysis for all reported results are provided in Supplementary Note 4. Sample size for animal experiments was determined by power analysis using G*Power software. In all other experiments performed, no statistical methods were used to pre-determine sample sizes, but our sample sizes are similar to those reported in previous publications[3,6,8,17]. No data were excluded from the analyses. No method of randomization was used, except for simple randomization applied for mice splitting in the murine melanoma models. Evaluation of microscopy analyses and animal experiments was performed by blinded evaluators. Reproducibility in all experiments was confirmed by performing at least three independent biological/chemical replicates.

Reporting summary

Further information on research design is available in the Nature Portfolio Reporting Summary linked to this article.

Data availability

Any additional information required to reanalyze the data presented in this paper is available from the lead contact upon reasonable request.

References

1. Gorgoulis, V. et al. Cellular senescence: defining a path forward. *Cell* **31**, 813–827 (2019).
2. Ogrodnik, M. et al. Guidelines for minimal information on cellular senescence experimentation in vivo. *Cell* **187**, 4150–4175 (2024).
3. Zampetidis, C. P. et al. A recurrent chromosomal inversion suffices for driving escape from oncogene-induced senescence via subTAD reorganization. *Mol. Cell* **81**, 4907–4923 (2021).
4. Bartkova, J. et al. Oncogene-induced senescence is part of the tumorigenesis barrier imposed by DNA damage checkpoints. *Nature* **444**, 633–637 (2006).
5. Halazonetis, T. D., Gorgoulis, V. G. & Bartek, J. An oncogene-induced DNA damage model for cancer development. *Science* **319**, 1352–1355 (2008).
6. Evangelou, K., Belogiannis, K., Papaspyropoulos, A., Petty, R. & Gorgoulis, V. G. Escape from senescence: molecular basis and therapeutic ramifications. *J. Pathol.* **260**, 649–665 (2023).
7. Demaria, M. et al. Cellular senescence promotes adverse effects of chemotherapy and cancer relapse. *Cancer Discov.* **7**, 165–176 (2017).
8. Galanos, P. et al. Chronic p53-independent p21 expression causes genomic instability by deregulating replication licensing. *Nat. Cell Biol.* **18**, 777–789 (2016).
9. Wang, B., Kohli, J. & Demaria, M. Senescent cells in cancer therapy: friends or foes? *Trends Cancer.* **6**, 838–857 (2020).
10. Myrianthopoulos, V. et al. Senescence and senotherapeutics: a new field in cancer therapy. *Pharmacol. Ther.* **193**, 31–49 (2019).
11. Wang, L., Lankhorst, L. & Bernards, R. Exploiting senescence for the treatment of cancer. *Nat. Rev. Cancer* **22**, 340–355 (2022).
12. Zhu, Y. et al. The Achilles' heel of senescent cells: from transcriptome to senolytic drugs. *Aging Cell* **14**, 644–658 (2015).
13. Chaib, S., Tchkonia, T. & Kirkland, J. L. Cellular senescence and senolytics: the path to the clinic. *Nat. Med.* **28**, 1556–1568 (2022).
14. Schmitt, C. A., Wang, B. & Demaria, M. Senescence and cancer—role and therapeutic opportunities. *Nat. Rev. Clin. Oncol.* **19**, 619–636 (2022).
15. Kohli, J. et al. Algorithmic assessment of cellular senescence in experimental and clinical specimens. *Nat. Protoc.* **16**, 2471–2498 (2021).
16. Kirkland, J. L. & Tchkonia, T. Senolytic drugs: from discovery to translation. *J. Intern. Med.* **288**, 518–536 (2020).
17. Magkouta, S. et al. A fluorophore-conjugated reagent enabling rapid detection, isolation and live tracking of senescent cells. *Mol. Cell* **83**, 3558–3573 (2023).
18. Sachs, N. et al. Long-term expanding human airway organoids for disease modeling. *EMBO J.* **38**, e100300 (2019).
19. Vilgelm, A. E. et al. Connecting the dots: therapy-induced senescence and a tumor-suppressive immune microenvironment. *J. Natl Cancer Inst.* **108**, djv406 (2015).
20. McGrath, N. A., Andersen, K. A., Davis, A. K., Lomax, J. E. & Raines, R. T. Diazo compounds for the bioreversible esterification of proteins. *Chem. Sci.* **6**, 752–755 (2015).
21. Evangelou, K. et al. Robust, universal biomarker assay to detect senescent cells in biological specimens. *Aging Cell* **16**, 192–197 (2017).
22. Liederer, B. M. & Borchardt, R. T. Enzymes involved in the bioconversion of ester-based prodrugs. *J. Pharm. Sci.* **95**, 1177–1195 (2006).
23. Kawakami, S., Johmura, Y. & Nakanishi, M. Intracellular acidification and glycolysis modulate inflammatory pathway in senescent cells. *J. Biochem.* **176**, 97–108 (2024).
24. Immordino, M. L., Dosio, F. & Cattel, L. Stealth liposomes: review of the basic science, rationale, and clinical applications, existing and potential. *Int. J. Nanomedicine* **1**, 297–315 (2006).
25. Zeng, X. et al. Construction of pH-sensitive targeted micelle system co-delivery with curcumin and dasatinib and evaluation of anti-liver cancer. *Drug Deliv.* **29**, 792–806 (2022).
26. Shyam Sunder, S., Sharma, U. C. & Pokharel, S. Adverse effects of tyrosine kinase inhibitors in cancer therapy: pathophysiology, mechanisms and clinical management. *Signal. Transduct. Target. Ther.* **8**, 262 (2023).
27. Sena, M. C. et al. Chronic consumption of distilled sugarcane spirit induces anxiolytic-like effects in mice. *Clinics (Sao Paulo)* **66**, 873–878 (2011).
28. Gasek, N. S., Kuchel, G. A., Kirkland, J. L. & Xu, M. Strategies for targeting senescent cells in human disease. *Nat. Aging* **1**, 870–879 (2021).
29. Lee, B. Y. et al. Senescence-associated β-galactosidase is lysosomal β-galactosidase. *Aging Cell* **5**, 187–195 (2006).
30. Adamczyk-Grochala, J. & Lewinska, A. Nano-based theranostic tools for the detection and elimination of senescent cells. *Cells* **9**, 2659 (2020).
31. López-Otín, C., Blasco, M. A., Partridge, L., Serrano, M. & Kroemer, G. Hallmarks of aging: an expanding universe. *Cell* **186**, 243–278 (2023).
32. Sapieha, P. & Mallette, F. A. Cellular senescence in postmitotic cells: beyond growth arrest. *Trends Cell Biol.* **28**, 595–607 (2018).
33. von Zglinicki, T., Wan, T. & Miwa, S. Senescence in post-mitotic cells: a driver of aging? *Antioxid. Redox Signal.* **34**, 308–323 (2021).
34. Baker, D. J. et al. Clearance of $p16^{Ink4a}$-positive senescent cells delays ageing-associated disorders. *Nature* **479**, 232–236 (2011).
35. Binkhathlan, Z., Ali, R., Qamar, W. & Lavasanifar, A. Pharmacokinetics of orally administered poly(ethylene oxide)-*block*-poly(ε-caprolactone) micelles of cyclosporine A in rats: comparison with Neoral®. *J. Pharm. Pharm. Sci.* **21**, 192s–199s (2018).
36. Binkhathlan, Z. & Lavasanifar, A. in *Nanoarchitectonics in Biomedicine* Ch. 15 (ed. Grumezescu, A. M.) 507–546 (William Andrew Publishing, 2019).
37. Binkhathlan, Z., Ali, R., Qamar, W., Al-Lawati, H. & Lavasanifar, A. Pharmacokinetic and tissue distribution of orally administered cyclosporine A-loaded poly(ethylene oxide)-*block*-poly(ε-caprolactone) micelles versus Sandimmune® in rats. *Pharm. Res.* **38**, 51–65 (2021).
38. Molavi, O. et al. Polymeric micelles for the solubilization and delivery of STAT3 inhibitor cucurbitacins in solid tumors. *Int. J. Pharm.* **347**, 118–127 (2008).
39. Soleimani, A. H. et al. Micellar nano-carriers for the delivery of STAT3 dimerization inhibitors to melanoma. *Drug Deliv. Transl. Res.* **7**, 571–581 (2017).
40. Garg, S. M., Vakili, M. R. & Lavasanifar, A. Polymeric micelles based on poly(ethylene oxide) and α-carbon substituted poly(ε-caprolactone): an in vitro study on the effect of core forming block on polymeric micellar stability, biocompatibility, and immunogenicity. *Colloids Surf. B Biointerfaces* **132**, 161–170 (2022).
41. Dookun, E., Passos, J. F., Arthur, H. M. & Richardson, G. D. Therapeutic potential of senolytics in cardiovascular disease. *Cardiovasc. Drugs Ther.* **36**, 187–196 (2022).
42. Barnes, P. J., Baker, J. & Donnelly, L. E. Cellular senescence as a mechanism and target in chronic lung diseases. *Am. J. Respir. Crit. Care Med.* **200**, 556–564 (2019).

43. Wyld, L. et al. Senescence and cancer: a review of clinical implications of senescence and senotherapies. *Cancers (Basel)* **12**, 2134 (2020).
44. Zhu, Y. et al. New agents that target senescent cells: the flavone, fisetin, and the BCL-X_L inhibitors, A1331852 and A1155463. *Aging (Albany NY)* **9**, 955–963 (2017).
45. Schoenwaelder, S. M. et al. Bcl-x_L-inhibitory BH3 mimetics can induce a transient thrombocytopathy that undermines the hemostatic function of platelets. *Blood* **118**, 1663–1674 (2011).
46. Angelopoulou, A. et al. Loss of the tumour suppressor LKB1/STK11 uncovers a leptin-mediated sensitivity mechanism to mitochondrial uncouplers for targeted cancer therapy. *Mol. Cancer* **23**, 147 (2024).
47. Mourkioti, I. et al. A GATA2-CDC6 axis modulates androgen receptor blockade-induced senescence in prostate cancer. *J. Exp. Clin. Cancer Res.* **42**, 187 (2023).
48. Zampetidis, C. P., Papantonis, A. & Gorgoulis, V. G. Escape from senescence: revisiting cancer therapeutic strategies. *Mol. Cell. Oncol.* **9**, 2030158 (2022).
49. Pippa, N., Deli, E., Mentzali, E., Pispas, S. & Demetzos, C. PEO-b-PCL grafted DPPC liposomes: physicochemical characterization and stability studies of novel bio-inspired advanced Drug Delivery nano Systems (aDDnSs). *J. Nanosci. Nanotechnol.* **14**, 5676–5681 (2014).
50. Faul, F., Erdfelder, E., Lang, A. G. & Buchner, A. G*Power 3: a flexible statistical power analysis program for the social, behavioral, and biomedical sciences. *Behav. Res. Methods.* **39**, 175–191 (2007).
51. Schafer, M. J. et al. Cellular senescence mediates fibrotic pulmonary disease. *Nat. Commun.* **8**, 14532 (2017).
52. Novais, E. J. et al. Long-term treatment with senolytic drugs dasatinib and quercetin ameliorates age-dependent intervertebral disc degeneration in mice. *Nat. Commun.* **12**, 5213 (2021).
53. Korashy, H. M., Rahman, A. F. & Kassem, M. G. Dasatinib. *Profiles Drug Subst. Excip. Relat. Methodol.* **39**, 205–237 (2014).

Acknowledgements

We acknowledge support by the National Public Investment Program of the Ministry of Development and Investment/General Secretariat for Research and Technology, in the framework of the Flagship Initiative to address SARS-CoV-2 (2020ΣΕ01300001; V.G.G.); a Sonia & Nikos Kotopoulos Trust donation (V.G.G.); and Hellenic Foundation for Research and Innovation grant 3782 (V.G.G.). The cryo-EM work was supported by the Hellenic Foundation for Research and Innovation under the '1st Call for H.F.R.I. Research Projects to support Faculty members and Researchers and the procurement of high-cost research equipment' (project no: 2906; V.G.G.); NKUA-SARG grant 70/3/8916 (V.G.G.); and the Foundation for Education and European Culture (A. Papaspyropoulos).

Author contributions

S.M. and D.V.: cell culture and in vitro assays. D.V.: immunofluorescence staining. D.V. and K.K.: confocal microscopy. K.E. and V.G.G.: histopathological examination and staining evaluation. S.M.: murine models. A. Papaspyropoulos: organoid isolation and development. V.G.G. and N. Lougiakis: chemical design of GL392. M.G.: chemical synthesis of GL392 compound, purification of GL392 and intermediates by flash chromatography and TLC analyses. M.G., N. Pouli, P.M. and N. Lougiakis: chemical synthesis of GL392 compound; structural characterization of all compounds by 1H NMR, 13C NMR and 2D spectra; mass spectroscopy; and determination of melting points. A. Palaiologou and C.T.: LC–MS experiments. N. Pippa and N. Lagopati: micelle design. N. Pippa, N. Lagopati, N.B. and S.H.: micelle characterization. S.P. and N.P.: micelle synthesis. S.M., D.V. and A. Papaspyropoulos: micelle validation. S.M., D.V., A. Papaspyropoulos, N. Lagopati, D.-F.T., A.K. and K.E.: data analysis, statistical analysis, interpretation of results and manuscript preparation. F.S., D.T., R.P., N.K., K.E. and V.G.G.: experimental design and guidance. K.E. and V.G.G.: manuscript writing, with input from all co-authors. V.G.G.: project conceptualization, resources, funding and supervision of experiments.

Competing interests

Described compounds are in patent pending status: (1) Greek Patent Application No. 20240100309, (2) UK Patent Application No. GB2406749.8 and (3) international Patent Cooperation Treaty filing. Patent competing interests concern N.K. and V.G.G. only. The other authors declare no competing interests.

Additional information

Extended data is available for this paper at https://doi.org/10.1038/s43587-024-00747-4.

Supplementary information The online version contains supplementary material available at https://doi.org/10.1038/s43587-024-00747-4.

Correspondence and requests for materials should be addressed to Vassilis G. Gorgoulis.

Peer review information *Nature Aging* thanks Yizhou Dong, Gerardo Ferbeyre Guangrong Zheng and the other, anonymous, reviewer(s) for their contribution to the peer review of this work.

https://doi.org/10.1038/s43587-024-00747-4

[1]Molecular Carcinogenesis Group, Department of Histology and Embryology, Medical School, National and Kapodistrian University of Athens, Athens, Greece. [2]Marianthi Simou and G.P. Livanos Labs, 1st Department of Critical Care and Pulmonary Services, School of Medicine, National & Kapodistrian University of Athens,'Evangelismos' Hospital, Athens, Greece. [3]Ninewells Hospital and Medical School, University of Dundee, Dundee, UK. [4]Division of Pharmaceutical Chemistry, Department of Pharmacy, School of Health Sciences, National and Kapodistrian University of Athens, Panepistimiopolis Zografou, Athens, Greece. [5]Section of Pharmaceutical Technology, Department of Pharmacy, School of Health Sciences, National and Kapodistrian University of Athens, Panepistimioupolis Zografou, Athens, Greece. [6]Center of Clinical, Experimental Surgery & Translational Research, Biomedical Research Foundation of the Academy of Athens, Athens, Greece. [7]Hellenic Pasteur Institute, Athens, Greece. [8]Laboratory of Biology, Department of Basic Medical Sciences, Medical School, National and Kapodistrian University of Athens, Athens, Greece. [9]Biomedical Research Foundation, Academy of Athens, Athens, Greece. [10]Institute of Nanoscience and Nanotechnology, National Center for Scientific Research 'Demokritos', Agia Paraskevi, Greece. [11]Wellcome-MRC Cambridge Stem Cell Institute, Cambridge, UK. [12]Cambridge Liver Unit, Cambridge University Hospitals NHS Foundation Trust, Cambridge, UK. [13]Department of Medicine, University of Cambridge, Cambridge, UK. [14]Theoretical and Physical Chemistry Institute, National Hellenic Research Foundation, Athens, Greece. [15]Faculty Institute for Cancer Sciences, Manchester Academic Health Sciences Centre, University of Manchester, Manchester, UK. [16]Intelligencia, Inc., New York, NY, USA. [17]These authors contributed equally: Sophia Magkouta, Dimitris Veroutis, Angelos Papaspyropoulos, Maria Georgiou. ✉e-mail: vgorg@med.uoa.gr

https://doi.org/10.1038/s43587-024-00747-4

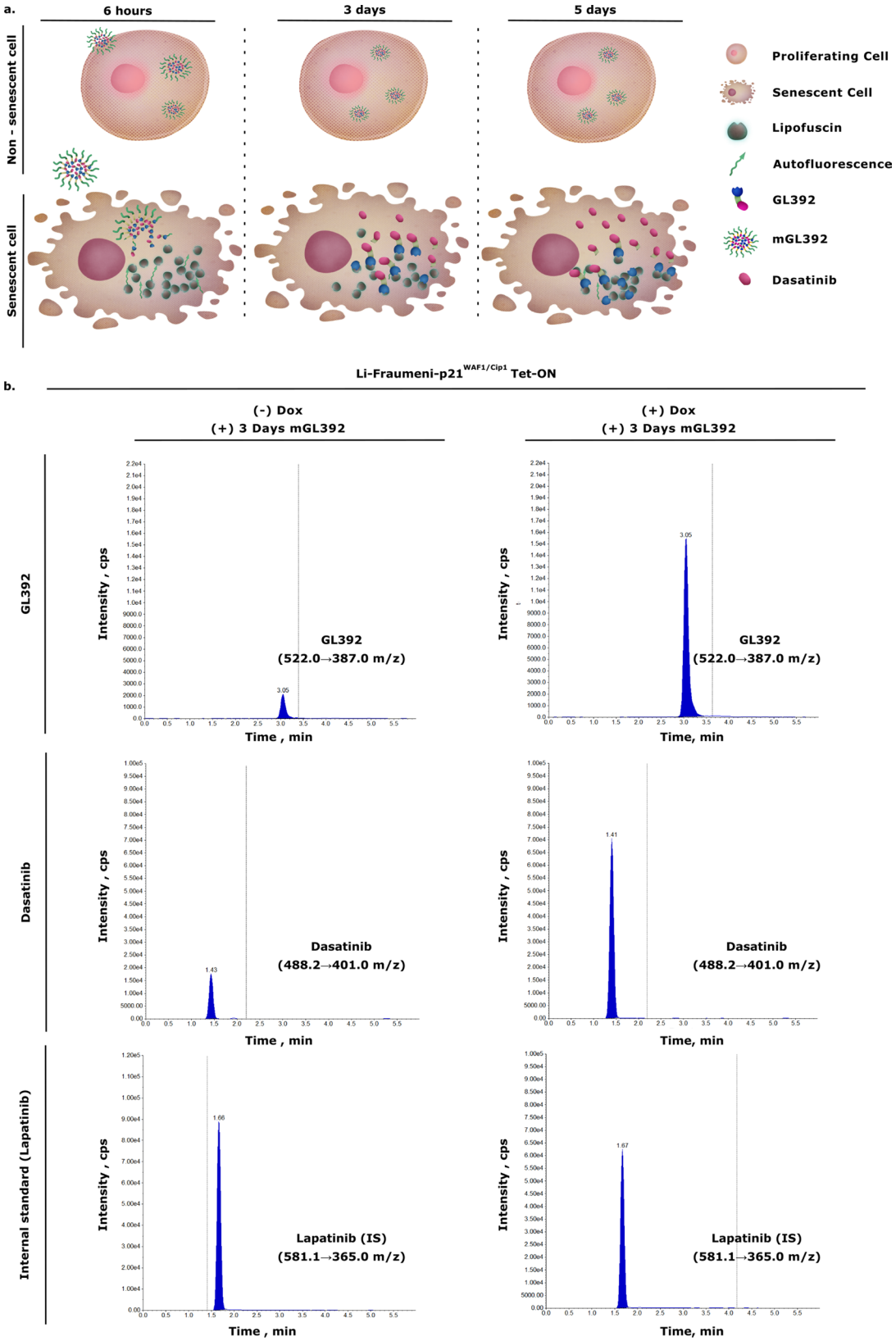

Extended Data Fig. 1 | mGL392 selectively delivers GL392 in senescent cells followed by Dasatinib release. (**a**) Schematic representation of the dynamic process of Dasatinib release. mGL392 preferably enters senescent cells delivering its GL392 cargo. Dasatinib release initiates 6 h upon mGL392 treatment and peaks 3 days later. (**b**) Representative output of LC-MS analysis of senescent (+Dox) versus non- senescent (-Dox) Li-Fraumeni-p21$^{WAF1/Cip1}$ Tet-ON cell lysates from cells treated with mGL392 for 3 days. Peaks depict relative abundance of the released GL392 and the released Dasatinib traced in the cell lysates. Peaks were identified based on prepared GL392 and Dasatinib stock solutions. Lapatinib served as an internal standard of the analysis.

https://doi.org/10.1038/s43587-024-00747-4

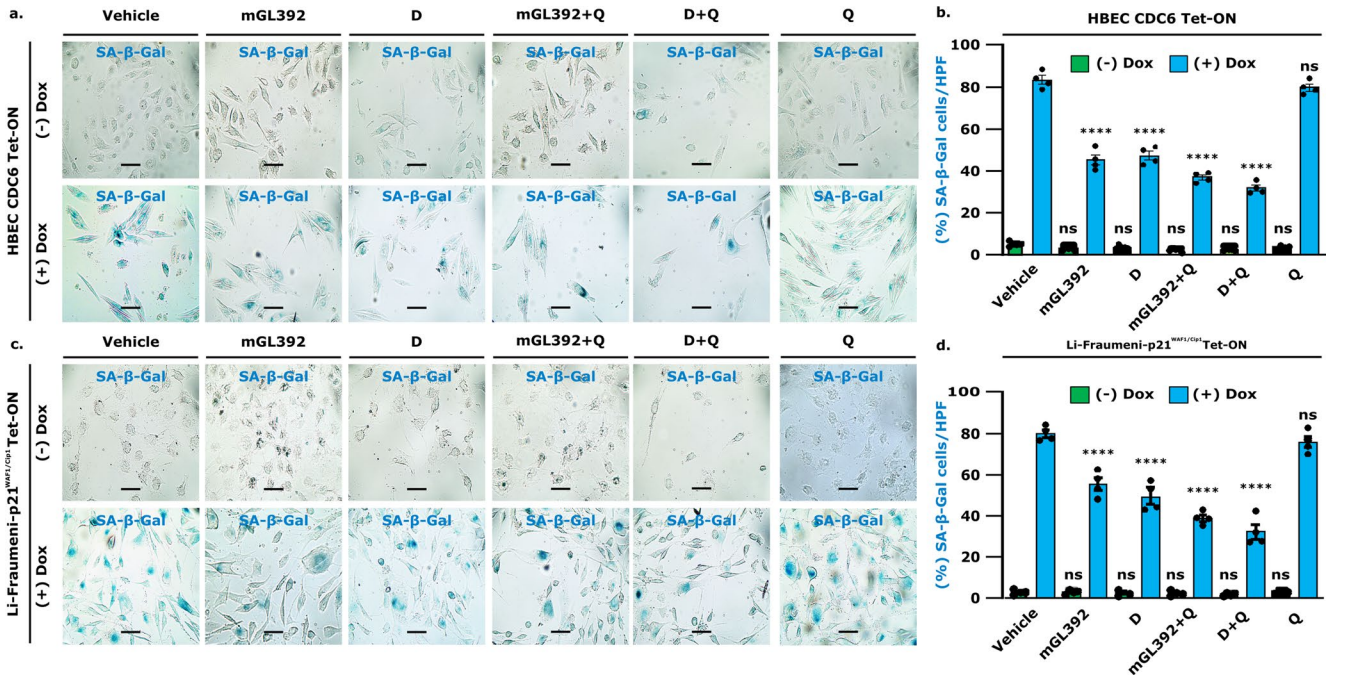

Extended Data Fig. 2 | Verification of mGL392-induced senolysis by SA-β-gal staining. HBEC CDC6 Tet-ON (**a**, **b**) and Li-Fraumeni-p21$^{WAF1/Cip1}$ Tet-ON (**c**, **d**) cells entered senescence upon Doxycycline (Dox) treatment. Senescent and respective non-senescent counterparts were subsequently treated with Vehicle (PBS), mGL392 (10 nM in the case of HBEC CDC6 Tet-ON and 20 nM in the case of Li-Fraumeni-p21$^{WAF1/Cip1}$ Tet-ON cells) or mGL392+Quercetin (mGL392+Q, 10 or 20 nM and 10 μM, respectively), free Dasatinib (D, 10 and 20 nM for HBEC CDC6 Tet-ON and Li-Fraumeni-p21$^{WAF1/Cip1}$ Tet-ON cells, respectively), Quercetin (Q, 10 μM) and free Dasatinib+Quercetin (D + Q) for 4-6 days and stained for SA-β-gal. (**a**, **c**) Representative images. Objective 20x. Scale bar: 10 μm. (**b**, **d**) Quantification of SA-β-gal(+) cells, n = 4 (biological replicates), **** $p < 0.0001$ compared to respective vehicle, two-way ANOVA test. Error bars indicate SD. Data expressed are presented as mean values ± SEM.

https://doi.org/10.1038/s43587-024-00747-4

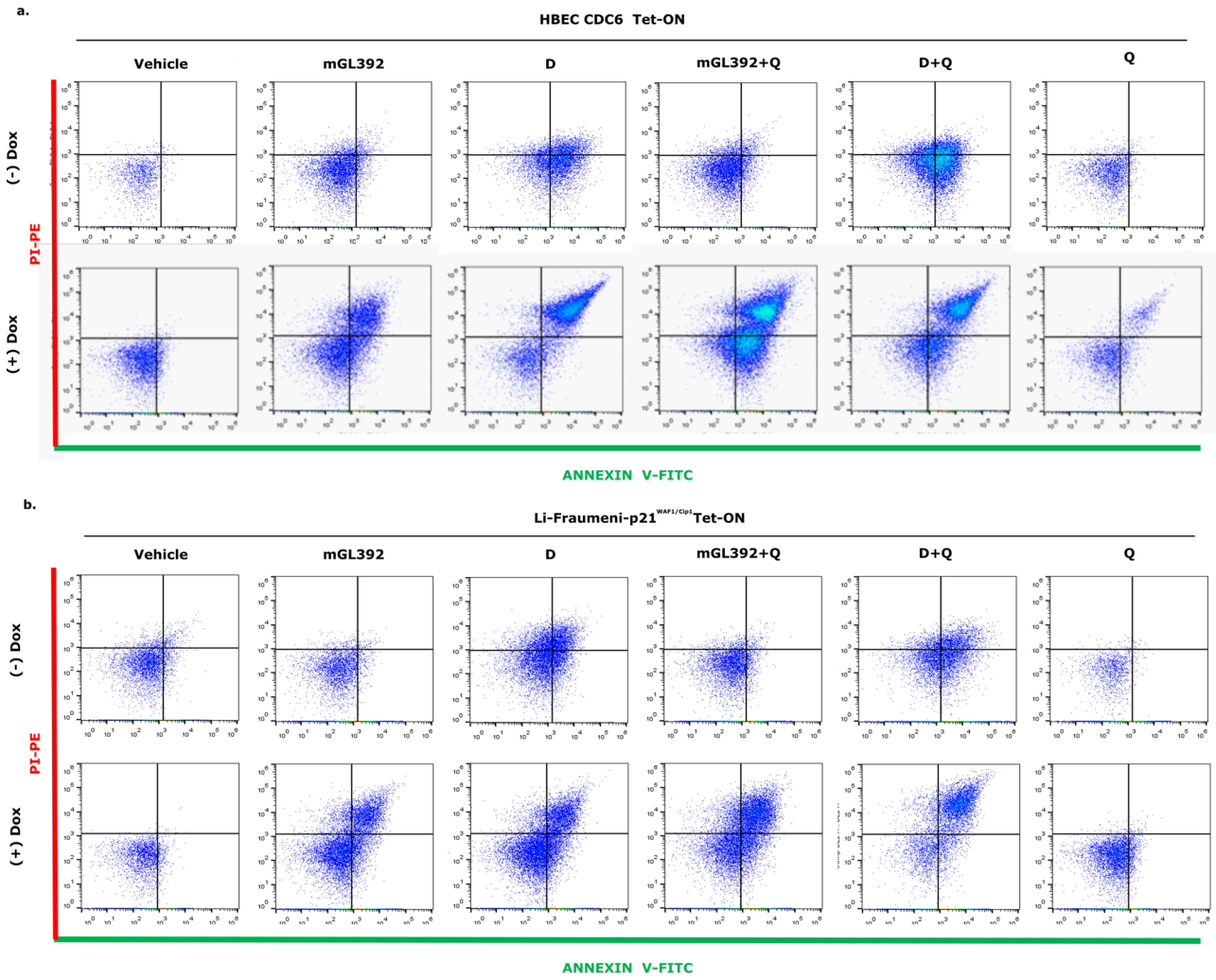

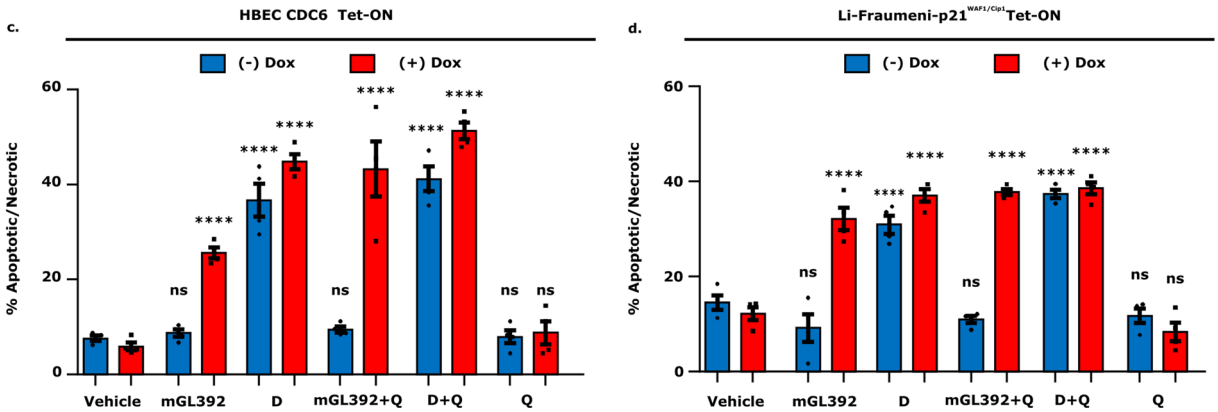

Extended Data Fig. 3 | Verification of mGL392-induced senolytic activity via flow cytometry-based apoptotic assessment. HBEC CDC6 Tet-ON (**a**, **c**) and Li-Fraumeni-p21$^{WAF1/Cip1}$ Tet-ON (**b**, **d**) cells were treated with Doxycycline (Dox) to induce senescence. Senescent cells and their non-senescent counterparts were treated with Vehicle (PBS), mGL392 (10 nM in the case of HBEC CDC6 Tet-ON and 20 nM in the case of Li-Fraumeni-p21$^{WAF1/Cip1}$ Tet-ON cells) or mGL392+Quercetin (mGL392+Q, 10 or 20 nM and 10 μM, respectively), free Dasatinib (D, 10 and 20 nM for HBEC CDC6 Tet-ON and Li-Fraumeni-p21$^{WAF1/Cip1}$ Tet-ON cells, respectively), Dasatinib+Quercetin (D + Q, 10 or 20 nM and 10 μM, respectively) and Quercetin (Q, 10 μM) for 4-6 days and subsequently stained with Annexin V-FITC and PI for evaluation of apoptotic and dead cells, respectively. (**a**, **b**) Representative density plots from flow cytometry analysis. (**c**, **d**) Quantification of flow cytometry results presented as mean ± SEM, n = 4 (biological replicates), **** $p < 0.0001$; n.s. non-significant compared to respective vehicle by two-way ANOVA. Data expressed are presented as mean values ± SEM.

https://doi.org/10.1038/s43587-024-00747-4

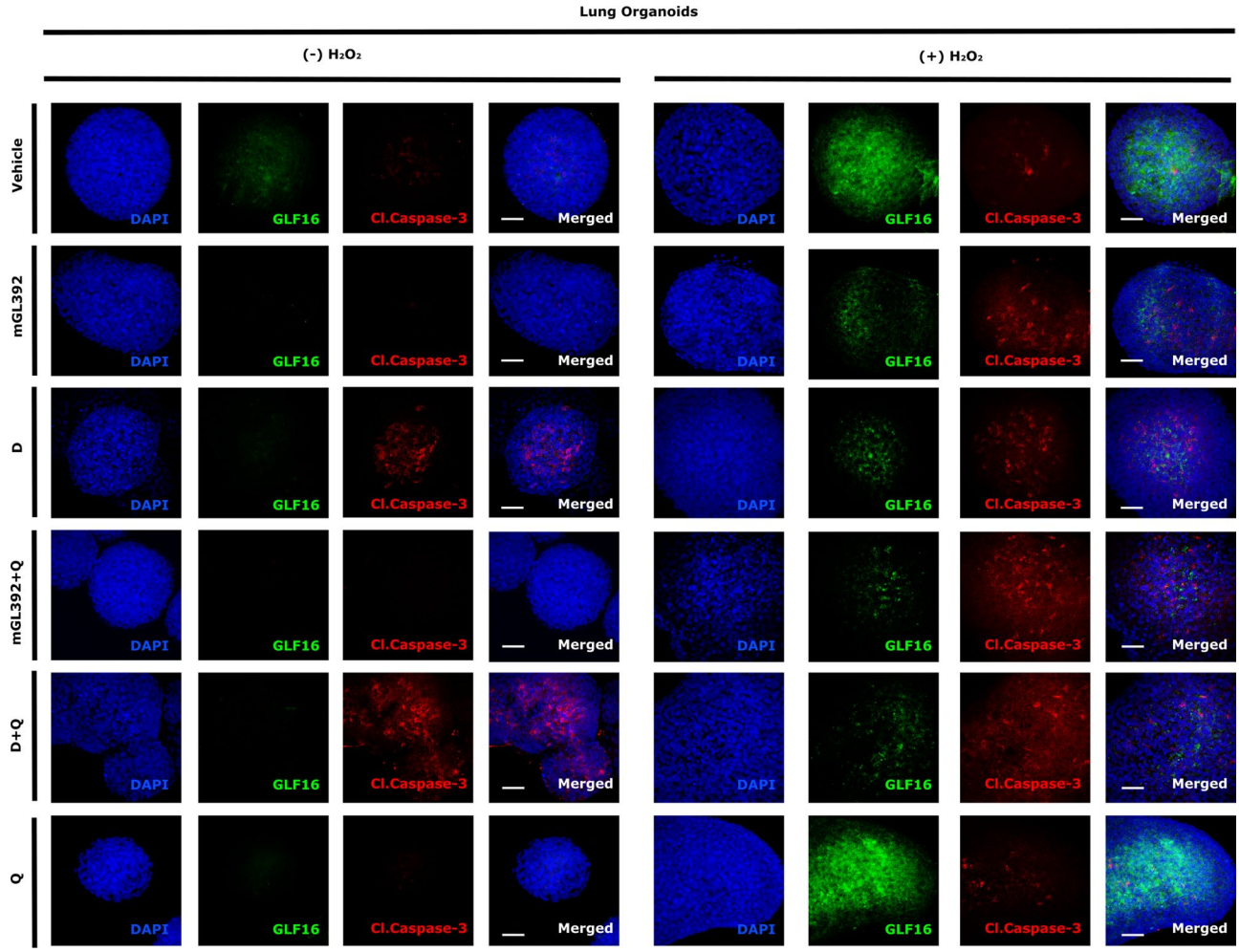

Extended Data Fig. 4 | Lung organoid stainings directly comparing mGL392 treatment with free agents. Individual staining panels of organoids from Fig. 6c. From left to right, representative split-channel image overlays of DAPI (blue), GLF16 (green) and Cl. Caspase-3 (red) staining, and respective composites. Objective 20x. Scale bar: 10 µm. Data shown are presented as mean values ± SD from 3 independent biological replicates.

https://doi.org/10.1038/s43587-024-00747-4

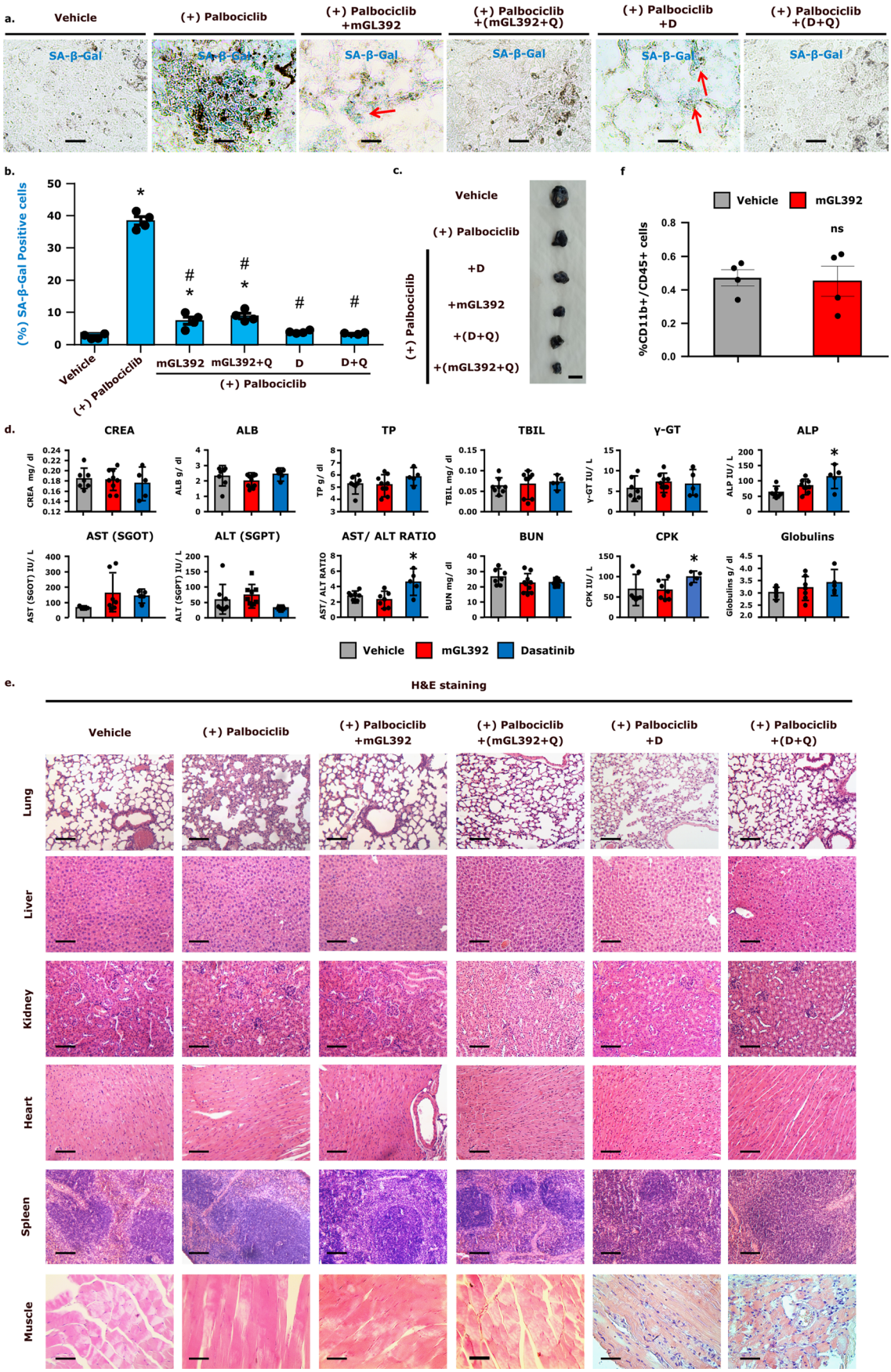

Extended Data Fig. 5 | See next page for caption.

https://doi.org/10.1038/s43587-024-00747-4

Extended Data Fig. 5 | In vivo administration of mGL392 effectively eliminates SA-β-gal(+) cells in the tumor without conferring cytotoxicity. (**a**) Representative pictures of excised mouse tumors stained for SA-β-gal and (**b**) quantification of SA-β-gal(+) cells in (**a**) (n = 4, biological replicates). (**c**) Representative tumors from Fig. 7i, Scale bar: 5 mm. (**d**) Sera of vehicle (normal saline), mGL392 and Dasatinib-treated mice were analyzed for common toxicology markers associated with vital organ damage. Results are expressed as mean ± SD (n = 9 biological replicates). CREA: Creatinine; ALB: Albumin; TP: Total Protein; TBIL: Total Bilirubin; ALP: Alkaline Phosphatase; γ-GT: γ-glutamyltransferase; ALT: Alanine Transaminase; AST: Aspartate Aminotransferase; BUN: Blood Urea Nitrogen; CPK: Creatine Phosphokinase. (**e**) Vital organs (lung, liver, kidney, heart, spleen) and hindlimb muscle samples of all mice were excised and stained with hematoxylin and eosin for histopathological evaluation. (**f**) Monocyte populations in the blood of mice receiving vehicle (normal saline) or mGL392 were quantified using flow cytometry and found unaffected, n = 4 (biological replicates). Data are presented as mean values +/−SEM, *p < 0.05 compared to vehicle, #p < 0.05 compared to Palbociclib. n.s.; non-significant. Two-way ANOVA test (**b**), one-way ANOVA test (**d**), two-sided t-test (**f**) were used. Objectives 10x, 20x. Scale bars: 50 µm and 10 µm.

nature portfolio

Corresponding author(s): Vassilis G Gorgoulis

Last updated by author(s): Oct 3rd 2024

Reporting Summary

Nature Portfolio wishes to improve the reproducibility of the work that we publish. This form provides structure for consistency and transparency in reporting. For further information on Nature Portfolio policies, see our Editorial Policies and the Editorial Policy Checklist.

Statistics

For all statistical analyses, confirm that the following items are present in the figure legend, table legend, main text, or Methods section.

n/a	Confirmed
☐	☒ The exact sample size (*n*) for each experimental group/condition, given as a discrete number and unit of measurement
☐	☒ A statement on whether measurements were taken from distinct samples or whether the same sample was measured repeatedly
☐	☒ The statistical test(s) used AND whether they are one- or two-sided *Only common tests should be described solely by name; describe more complex techniques in the Methods section.*
☐	☒ A description of all covariates tested
☐	☒ A description of any assumptions or corrections, such as tests of normality and adjustment for multiple comparisons
☐	☒ A full description of the statistical parameters including central tendency (e.g. means) or other basic estimates (e.g. regression coefficient) AND variation (e.g. standard deviation) or associated estimates of uncertainty (e.g. confidence intervals)
☐	☒ For null hypothesis testing, the test statistic (e.g. *F*, *t*, *r*) with confidence intervals, effect sizes, degrees of freedom and *P* value noted *Give P values as exact values whenever suitable.*
☒	☐ For Bayesian analysis, information on the choice of priors and Markov chain Monte Carlo settings
☒	☐ For hierarchical and complex designs, identification of the appropriate level for tests and full reporting of outcomes
☒	☐ Estimates of effect sizes (e.g. Cohen's *d*, Pearson's *r*), indicating how they were calculated

Our web collection on statistics for biologists contains articles on many of the points above.

Software and code

Policy information about availability of computer code

Data collection	TEM cryo-samples pictures were observed with the Serial EM software.
Data analysis	i) GL392 purity analysis on HPLC was performed with the XcaliburTM 2.2 software, ii) autocorrelation functions for dynamic light scattering measurements were analyzed by the cumulant method and the CONTIN software, iii) LC-MS/MS data acquisition and processing was performed using Analyst software, iv) Flow cytometry data were analyzed with the FlowJo software v 10.8.1 package, v) auto-fluorescence images were quantified with Image J software, vi) statistical analyses were performed with GraphPad Prism software v10.0.

For manuscripts utilizing custom algorithms or software that are central to the research but not yet described in published literature, software must be made available to editors and reviewers. We strongly encourage code deposition in a community repository (e.g. GitHub). See the Nature Portfolio guidelines for submitting code & software for further information.

Data

Policy information about availability of data

All manuscripts must include a data availability statement. This statement should provide the following information, where applicable:

- Accession codes, unique identifiers, or web links for publicly available datasets
- A description of any restrictions on data availability
- For clinical datasets or third party data, please ensure that the statement adheres to our policy

The nature of the data generated in this report, does not require deposition in public repositories. The statement on data availability upon request concerns any potential explanations that may be requested on the data produced and described in the manuscript.

Research involving human participants, their data, or biological material

Policy information about studies with human participants or human data. See also policy information about sex, gender (identity/presentation), and sexual orientation and race, ethnicity and racism.

Reporting on sex and gender	No studies involving human participants were carried out. We received patient consent to use part of the tissue extracted for other medical purposes as a source to generate organoids. Use and further applications of organoids was irrelevant of the original patient. Collection of tissues for the generation of airway organoids was carried out according to the European Network of Research Ethics Committees (EUREC) guidelines and the local NKUA Medical School Bioethics committee (Protocol number: 571). All organoid lines were generated from patients who signed informed consent forms and their personal information remained anonymous.
Reporting on race, ethnicity, or other socially relevant groupings	No studies involving human participants were carried out
Population characteristics	No studies involving human participants were carried out
Recruitment	No studies involving human participants were carried out
Ethics oversight	No studies involving human participants were carried out

Note that full information on the approval of the study protocol must also be provided in the manuscript.

Field-specific reporting

Please select the one below that is the best fit for your research. If you are not sure, read the appropriate sections before making your selection.

☒ Life sciences ☐ Behavioural & social sciences ☐ Ecological, evolutionary & environmental sciences

For a reference copy of the document with all sections, see nature.com/documents/nr-reporting-summary-flat.pdf

Life sciences study design

All studies must disclose on these points even when the disclosure is negative.

Sample size	Sample size for experiments using animals was determined upon power analysis using GPower software (ref 50 in manuscript: Faul et al, 2009) (setting significance 0.05, effect size f 0.89 and power 0.80). In all other experiments performed, no statistical methods were used to pre-determine sample sizes, but our sample sizes are similar to those reported in previous publications (refs 3, 8, 17, 21 in the manuscript).
Data exclusions	No data were excluded from the analyses
Replication	A minimum of three replicates was always performed. Moreover in the case of the microscopy analyses (eg immunofluorescence) >10 different optical fields per experimental replicate were interrogated.
Randomization	Sample allocation into experimental groups was random
Blinding	Investigators were blinded to group allocation during data collection and during evaluations of results, particularly for microscopy analyses.

Reporting for specific materials, systems and methods

We require information from authors about some types of materials, experimental systems and methods used in many studies. Here, indicate whether each material, system or method listed is relevant to your study. If you are not sure if a list item applies to your research, read the appropriate section before selecting a response.

Materials & experimental systems

n/a	Involved in the study
☐	☒ Antibodies
☐	☒ Eukaryotic cell lines
☒	☐ Palaeontology and archaeology
☐	☒ Animals and other organisms
☒	☐ Clinical data
☒	☐ Dual use research of concern
☒	☐ Plants

Methods

n/a	Involved in the study
☒	☐ ChIP-seq
☐	☒ Flow cytometry
☒	☐ MRI-based neuroimaging

Antibodies

Antibodies used: Cleaved Caspase-3 (#9661, Cell Signalling), secondary antibody (Alexa Fluor® 488), goat anti-rabbit IgG H&L (Alexa Fluor® 488), 1/500, ab150077, polyclonal, Abcam.
Antibodies used in flow cytometry for blood and sera analysis: anti-CD45-APC-Cy7 (clone 30-F11, #103115), CD11b-FITC (#101205, clone M1/70), F4/80-PerCP (#123125, clone BM8), Ly6C-PE ((#128007, clone HK1.4) at a 1/100 dilution (all from Biolegend, San Diego, CA)

Validation: As recommended by the manufacturer: i) Cl. Caspase-3 validation for IHC analysis was performed using FFPE human tonsil tissue, ii) Cl.Caspase-3 validation for IF was performed using HT-29 cells, untreated or Staurosporine treated.
For flow cytometry, antibody validation was performed by using isotype controls, untreated samples, and negative and positive biological controls recommended by the manufacturer.

Eukaryotic cell lines

Policy information about cell lines and Sex and Gender in Research

Cell line source(s): Li-Fraumeni-p21WAF1/Cip1 Tet-ON, HBEC CDC6 Tet-ON, B16 melanoma cell line and primary T cells, patient-derived airway organoids (unknown sex).
Li-Fraumeni p21WAF1/Cip1 Tet-ON are described in Galanos et al, Nat Cell Biol 2016 (ref 8 in the manuscript).
BEC CDC6 Tet-ON are described in Zampetidis et al, Mol Cell 2021 (ref 3 in the manuscript) and Komseli et al, BMC Genomics 2018.

Authentication: STR authentification

Mycoplasma contamination: All cell lines used were tested negative for mycoplasma contamination

Commonly misidentified lines (See ICLAC register): No commonly misidentified lines were used in the study

Animals and other research organisms

Policy information about studies involving animals; ARRIVE guidelines recommended for reporting animal research, and Sex and Gender in Research

Laboratory animals: C57B/L6 syngeneic male and female mice (6-8 weeks old) were used.
Mice were housed under a 12 hr light/dark cycle, at a 22.5°C temperature and 55% humidity, receiving food and water ad libidum. Animals were acclimatized for 10 days before experiments. Mouse experiments were approved by the Veterinary Administration Bureau, Prefecture of Athens, Greece (Decision No: 854066, 15/07/2023) under compliance to the national law and the EU Directives. Sample size was determined upon power analysis using GPower software (Faul et al, 2009) (setting significance 0.05, effect size f 0.89 and power 0.80).

Wild animals: The study did not involve wild animals

Reporting on sex: Findings apply to both sexes. Animals of both sexes were included in study design

Field-collected samples: The study did not involve field-collected samples

Ethics oversight: Mouse experiments were approved by the Veterinary Administration Bureau, Prefecture of Athens, Greece (Decision No: 854066, 15/07/2023 in compliance with national laws and EU directives

Note that full information on the approval of the study protocol must also be provided in the manuscript.

Plants

Seed stocks	No plants were used in the study
Novel plant genotypes	No plants were used in the study
Authentication	No plants were used in the study

Flow Cytometry

Plots

Confirm that:

☒ The axis labels state the marker and fluorochrome used (e.g. CD4-FITC).

☒ The axis scales are clearly visible. Include numbers along axes only for bottom left plot of group (a 'group' is an analysis of identical markers).

☐ All plots are contour plots with outliers or pseudocolor plots.

☐ A numerical value for number of cells or percentage (with statistics) is provided.

Methodology

Sample preparation	CELLS WERE COLLECTED, WASHED WITH PBS AND STAINED WITH ANNEXIN V-PI APOPTOSIS KIT ((#640914 BIOLEGEND). MURINE BLOOD SAMPLES WERE CENTRIFUGED FOR TOTAL WHITE BLOOD CELL (WBC) COLLECTION, RED BLOOD CELLS WERE LYSED AND WBC WERE STAINED AS DESCRIBED IN METHODS
Instrument	thermo attune nxt flow cytometer
Software	Attune NxT software
Cell population abundance	No sorting was perfomed
Gating strategy	Gating strategies are presented in the supplementary information

☒ Tick this box to confirm that a figure exemplifying the gating strategy is provided in the Supplementary Information.